Available online at www.sciencedirect.com

ScienceDirect

Geochimica et Cosmochimica Acta 164 (2015) 403–427

Geochimica et Cosmochimica Acta

www.elsevier.com/locate/gca

Silicon isotope fractionation during silica precipitation from hot-spring waters: Evidence from the Geysir geothermal field, Iceland

Sonja Geilert [a,*], Pieter Z. Vroon [b], Nicole S. Keller [c], Snorri Gudbrandsson [c], Andri Stefánsson [c], Manfred J. van Bergen [a]

[a] Department of Earth Science, Utrecht University, Budapestlaan 4, 3584 CD Utrecht, Netherlands
[b] Faculty of Earth and Life Sciences, VU University, 1081 HV Amsterdam, Netherlands
[c] Institute of Earth Sciences, University of Iceland, Sturlugata 7, 101 Reykjavík, Iceland

Received 7 August 2014; accepted in revised form 28 May 2015; available online 4 June 2015

Abstract

This study aims to explore the extent and controls of silicon isotope fractionation in hot spring systems of the Geysir geothermal area (Iceland), a setting where sinter deposits are actively formed. The $\delta^{30}Si$ values of dissolved silica measured in the spring water and sampling sites along outflowing streams, covering a temperature range between 20 and 100 °C, were relatively constant around +0.2‰, whereas the $\delta^{30}Si$ signatures of associated opaline sinters from the streambeds were between −0.1‰ and −4.0‰, becoming progressively more negative in the downstream parts of the aprons. Here, the deposited sinters represent some of the most ^{30}Si depleted abiotically produced terrestrial materials documented to date. Compared to the data reported for Icelandic basalts, considered to be the source of the silicon, the $\delta^{30}Si$ values of the fluids and sinter deposits are higher and lower, respectively.

The resulting values for apparent solid–water isotope fractionation ($\Delta^{30}Si_{solid-water}$) decreased with decreasing temperature from ca. −0.7‰ at ~80 °C to −3.7‰ at ~20 °C, locally down to −4.4‰. This temperature relationship was reproducible in each of the investigated hot spring systems and is qualitatively consistent with recent findings in laboratory experiments on kinetic fractionation for a flowing fluid. However, the apparent fractionation magnitudes observed in the field are ca. −2‰ more negative and thus significantly larger. We infer that solid–water silicon isotope fractionation during deposition of amorphous silica from a flowing fluid correlates inversely with temperature, but is essentially a function of the precipitation rate, such that the fractionation factor decreases with increasing rate. As an important corollary, the effective fractionation behavior during precipitation of silica from saturated solutions is a system-dependent feature, which should be taken into account when using silicon isotopes for paleo-environmental reconstructions.

1. INTRODUCTION

Evidence for both biotic and abiotic controls of biogeochemical cycles involving silicon in marine and terrestrial environments (e.g., Wollast and Mackenzie, 1983; Tréguer et al., 1995; Conley, 2002; Tréguer and De La Rocha, 2013) has received substantial support from studies of its stable isotopes (^{28}Si, ^{29}Si, ^{30}Si) in recent decades (Douthitt, 1982; Ding et al., 1996; De La Rocha et al., 2000; Basile-Doelsch, 2006; Georg et al., 2006, 2007a; Opfergelt and Delmelle, 2012). Silicon isotopes are capable of revealing past and present patterns in the supply of silica to, or removal from natural aqueous solutions owing to

* Corresponding author at: GEOMAR Helmholtz Centre for Ocean Research Kiel, Wischhofstr. 1-3, 24148 Kiel, Germany. Tel.: +49 (0)431 600 2114.
E-mail address: sgeilert@geomar.de (S. Geilert).

http://dx.doi.org/10.1016/j.gca.2015.05.043
0016-7037/

their conspicuous fractionation behavior when fluid and solid matter interact. Biotic as well as abiotic silica formation is usually accompanied by preferential uptake of the lighter isotopes, yielding lower $\delta^{30}Si$ than the remaining fluid. As a consequence, there are noticeable differences in isotope compositions between crustal rocks, the ultimate source of silicon, and dissolved silica in Earth's main surface water reservoirs. Igneous rocks are relatively uniform in $\delta^{30}Si$, with values around −0.3‰ for mafic and ca. 0‰ for felsic equivalents, in line with magmatic differentiation tending to enrich a melt in the heavier Si isotopes (Douthitt, 1982; Ding et al., 1996; Ziegler et al., 2005a; Georg et al., 2007a,b; Abraham et al., 2011; Savage et al., 2010, 2011, 2013). On the other hand, $\delta^{30}Si$ signatures of soils and soil clays (−2.4 to +0.6‰) and silcretes (−5.7‰ to −1.6‰) show significant ranges extending toward more negative values (Ziegler et al., 2005a,b; Basile-Doelsch et al., 2005; Georg et al., 2009; Opfergelt et al., 2009, 2010; Opfergelt et al., 2012; Bern et al., 2010; Cornelis et al., 2010, 2014; Steinhoefel et al., 2011; Pogge von Strandmann et al., 2012), whereas values measured in river waters vary from near 0‰ to +3.4‰ (De La Rocha et al., 2000; Ding et al., 2004, 2011; Georg et al., 2007a; Cardinal et al., 2010; Engström et al., 2010; Hughes et al., 2013). These findings highlight the role of chemical weathering in creating isotopic heterogeneity in solid residues of water-rock interaction and in contributing to the positive $\delta^{30}Si$ signatures that mark the global continent-derived supply of dissolved silica to the oceans (e.g., De La Rocha et al., 2000; Ding et al., 2004; Georg et al., 2009; Bern et al., 2010; Opfergelt et al., 2010, 2012, 2013; Cornelis et al., 2011; Opfergelt and Delmelle, 2012).

Quantitative data on experimental Si isotope fractionation during mineral formation (here expressed as $\Delta^{30}Si_{solid-fluid} = \delta^{30}Si_{solid} - \delta^{30}Si_{fluid}$) associated with weathering are only available for kaolinite and allophane ($\Delta^{30}Si = -2‰$ and −1.8‰, respectively (Ziegler et al., 2005a,b). Experimental work on fractionation during abiotic precipitation or sorptive removal of amorphous silica from a solution has invariably confirmed the preferential uptake of the lighter isotopes by the solid. Batch experiments have inferred $\Delta^{30}Si_{solid-fluid}$ between −1‰ and −5‰ for these cases (Li et al., 1995; Delstanche et al., 2009; Oelze et al., 2014, 2015; Roerdink et al., 2015). From experiments simulating steady-state deposition from a flowing fluid, Geilert et al. (2014) inferred that magnitudes of apparent silicon isotope fractionations between precipitated and dissolved silica is a function of temperature, and found $\Delta^{30}Si_{solid-fluid}$ to vary between −2.1‰ at 10 °C and nearly insignificant at temperatures ⩾50 °C. Their findings suggest that effective Si isotope fractionation is subject to changes in the saturation state, reactive surface area and flow regime, i.e. factors with a bearing on the precipitation rate of amorphous silica.

Controlled laboratory experiments as mentioned above provide first guidelines for understanding isotope fractionation in systems with a continuous supply of silica depositing fluid, but they may be inadequate to fully encompass the intricate details of natural processes. Active hot-spring systems provide a unique opportunity for studying silicon isotope fractionation during silica precipitation from a supersaturated flowing solution under more complex field conditions. The formation of silica sinters is a widespread phenomenon where geothermal water of deep origin discharges and cools at the Earth's surface (Fournier and Rowe, 1966; Fournier, 1985; Williams and Crerar, 1985). The initial silica precipitation from supersaturated solutions typically produces non-crystalline opal-A (White et al., 1956; Jones and Segnit, 1971; Rice et al., 1995; Herdianita et al., 2000; Lynne and Campbell, 2003; Lynne et al., 2005). Since various environmental parameters have an influence on the precipitation process (Campbell et al., 2001; Guidry and Chafetz, 2002, 2003a,b; Renaut and Jones, 2003; Rodgers et al., 2004; Lynne et al., 2008; Tobler et al., 2008; Lynne, 2012; Tobler and Benning, 2013), it is conceivable that the same ambient conditions also play a controlling role in concomitant silicon isotope fractionation.

Silicon isotope data from natural hydrothermal fluids and associated deposits are scarce. Available $\delta^{30}Si$ values for terrestrial hot spring waters (−0.2 to +0.6) and mid-ocean ridge hydrothermal fluids (−0.2 and −0.4‰) span a narrow range (Douthitt, 1982; Ding et al., 1996; De La Rocha et al., 2000; Opfergelt et al., 2011, 2013) that roughly coincides with the compositions of igneous rocks. In contrast, the co-existing silica deposits exhibit a much larger spread between −3.1‰ and +0.5‰, (Douthitt, 1982; Ding et al., 1996; De La Rocha et al., 2000). This disparity is presumably attributable to fractionation effects but remains largely obscure to date.

A better knowledge of abiotic silicon isotope fractionation is not only important for understanding silicon isotope cycling in modern surface environments. It is also highly relevant for the use of silicon isotope data from siliceous chemical sediments as a paleoenvironment proxy in studies focusing on the Early Earth, given their probable abiotic formation in Archean and Early Proterozoic times. In recent years, much attention has been given to silicon isotope signatures of Precambrian cherts, aimed at deriving information on their depositional environment such as seawater temperature, provenance of the silica, the role of submarine hydrothermal input and early diagenetic processes (e.g., André et al., 2006; Robert and Chaussidon, 2006; Van den Boorn et al., 2007, 2010; Steinhoefel et al., 2009, 2010; Heck et al., 2011; Marin-Carbonne et al., 2011, 2012, 2014; Chakrabarti et al., 2012; Delvigne et al., 2012). Although significant progress has been made in this field, interpretations often suffer from incomplete insight into the magnitude and controls of solid–fluid Si isotopic fractionation. Studies of sinters from modern continental hot springs could alleviate this shortcoming, as they have been proposed as analogs for Archean cherts, despite that depositional environments and formation mechanisms may not have been identical in every respect (Konhauser and Ferris, 1996; Konhauser et al., 2001; Guidry and Chafetz, 2003a).

The Geysir geothermal field in Iceland is a well-studied geothermal area (e.g., Arnórsson, 1985; Kaasalainen and Stefánsson, 2012) where composition, salinity, pH and geochemical parameters of hot-spring waters issued at the

surface have been monitored over decades. Steep temperature gradients, easy access to sampling sites and relatively stable water chemistry (including high silica concentrations) turn the Geysir geothermal field into an ideal site for exploring silicon isotope fractionation in a natural setting. This paper presents the first study of silicon isotope compositions of its hot-spring waters and associated opal-A deposits. The results provide new constraints on silicon isotope fractionation during silica deposition from flowing fluids, and are used to discuss the underlying controls and implications for the interpretation of isotope data from orthochemical deposits aimed at environmental reconstructions.

2. GEYSIR GEOTHERMAL FIELD AND STUDY AREA

2.1. Field setting

Sinter deposits and associated hot spring waters and stream discharges were sampled at the Geysir geothermal field in the Southern Lowlands of Iceland. Geothermal activity is concentrated in a small area of about 3 km^2 at an elevation of ca. 120 m a.s.l. (Fig. 1), and is characterized by hot springs, geyser activity, steam vents and mud pools. Underlying rocks of basalts and rhyolite domes belong to the Brunhes magnetic epoch (i.e. younger than 700.000 yr). Water temperatures at the surface are between 20 and 100 °C, whereas aquifer temperatures at depth have been estimated at ~230–260 °C (Arnórsson, 1985; Kaasalainen and Stefánsson, 2012). Water types include NaCl-waters, steam-heated acid sulfate waters and mixtures with non-thermal shallow ground and surface water. The pH of the Geysir waters ranges between 3.3 and 9.1 at surface temperatures, and concentrations of total dissolved solids (TDS) are between 85 and 1177 ppm (Arnórsson, 1985; Kaasalainen and Stefánsson, 2012).

Three hot spring systems were investigated for this study: Geysir, Háihver and Konungshver. Figs. 1 and 2 show schematic maps and field images.

2.1.1. Geysir

The Geysir hot spring and its outlet stream are located near the eastern border of the geothermal area. The circular pool (diameter ~20 m) had a shallow, <2 cm high rim (Fig. 2a). The bottom was covered with grayish and whitish siliceous material, which hardened toward the rim and

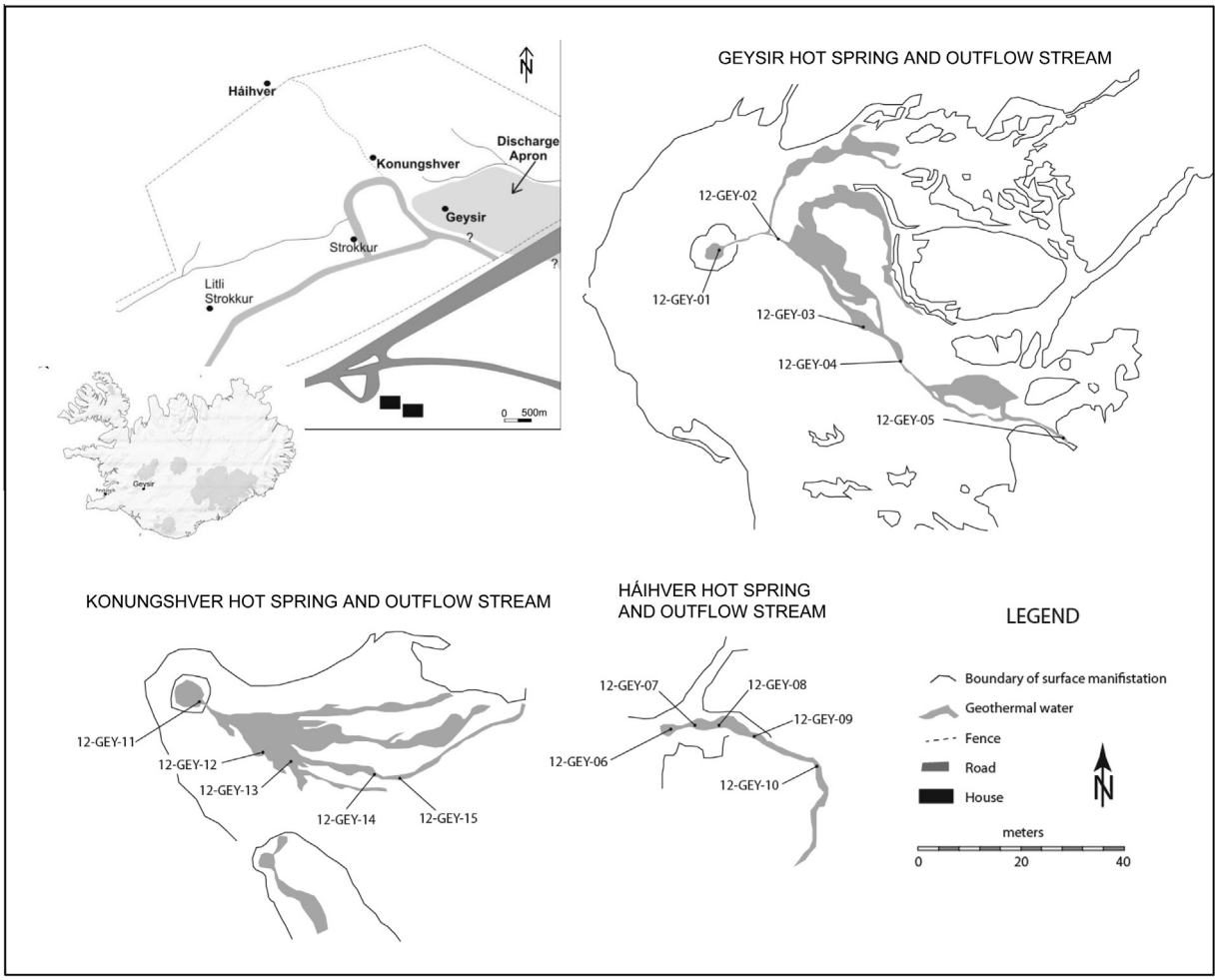

Fig. 1. Location of the Geysir geothermal area in Iceland, setting of the Geysir, Háihver and Konungshver hot spring systems, and sample locations.

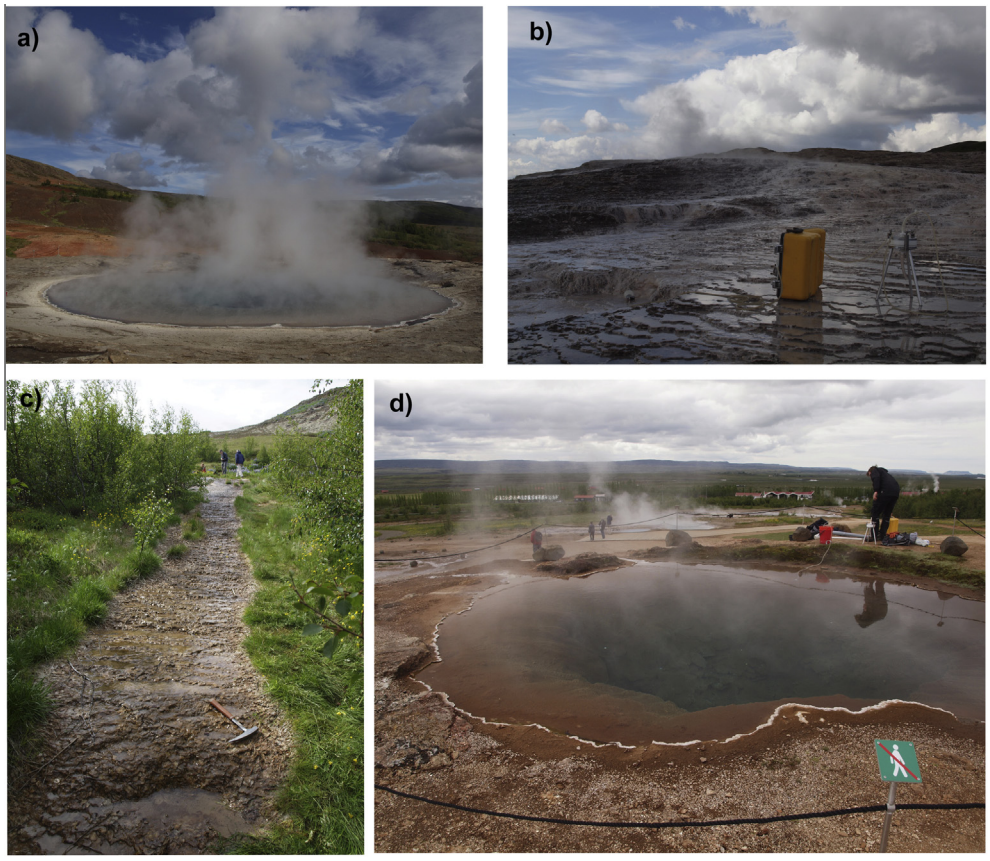

Fig. 2. Field impressions of the investigated hot-spring area. Near-circular spring pool (a) and terraced sinter deposits in the discharge stream (b) of Geysir; discharge channel of Háihver (c); spring pool with two outflow channels of Konungshver (d).

formed relatively homogeneous smooth siliceous crusts. The pool water had a temperature of ~90 °C.

A narrow outflow channel, about 10 cm deep, 33 cm wide and 1.5 m long, issued ca. 85 °C water. After this conduit, the stream broadened and flowed at an average rate of ~0.2 m s^{-1} across an area composed of siliceous, white terraces with local small pools and areas which had completely dried (Fig. 2b). Small rounded sinter knobs had formed in parts with less water exposure, apparently in response to repeated cycles of wetting and drying. The stream temperature decreased to ~20 °C over a distance of ~40 m (Fig. 3a), whereas the pH remained nearly constant around 9.3 (as measured at 20 °C) (Fig. 3b).

Subaqueous sinter in the streambed consisted of white to light gray, homogeneous, dense silica deposits with fine, up to ~3 mm thick laminae. In some parts, more irregular, ocher-greenish knobby material was covered by a white, dense, smooth silica crust. Locally, the crust showed a flow pattern in the form of parallel, elongated feather-like structures.

2.1.2. *Háihver*

The Háihver hot spring and its outflow stream are situated near the north-western rim of the area. The spring was oval (max. ~2 m across) and had a steep, ca. 30 cm high border. Siliceous sediments had a gray or brownish appearance and were coated with a hard siliceous crust. Average temperatures were ~100 °C but fluctuated due to episodic, violent surges, which also affected outflow rates. Surge amplitudes reached heights of some 15 cm. Surge cycles were irregular and included periods of stronger or weaker bubbling.

The first two meters of the single outflow channel were narrow (~20 cm wide) with a flow rate of ~1 m s^{-1}. The bottom was covered with sediments similar to those present in the pool. The water temperature (ca. 90 °C) fluctuated by about 10 °C, caused by the surges of the spring. After this stretch, the outflow channel broadened to a 2–3 m wide stream which passed terraces of hard brownish siliceous sediment and silicified leaves (Fig. 2c). The stream followed a rather steep slope where the flow rate was on average ~0.5 m s^{-1}. The borders were flat (<5 cm) and merged into adjacent grassy soil. The water temperature decreased to 23 °C over a distance of ~16 m (Fig. 3a). The pH increased slightly downstream from 8.9 to 9.2 (as measured at 20 °C) (Fig. 3b).

Sinter deposits in the stream bed were composed of alternating brownish-ocher and whitish laminae which were ⩽3 mm thick. The white layers showed feather-like, dense structures as in the Geysir stream deposits, whereas the brownish-ocher ones appeared more porous and heterogeneous. Covering crusts exhibited small spicules. In the

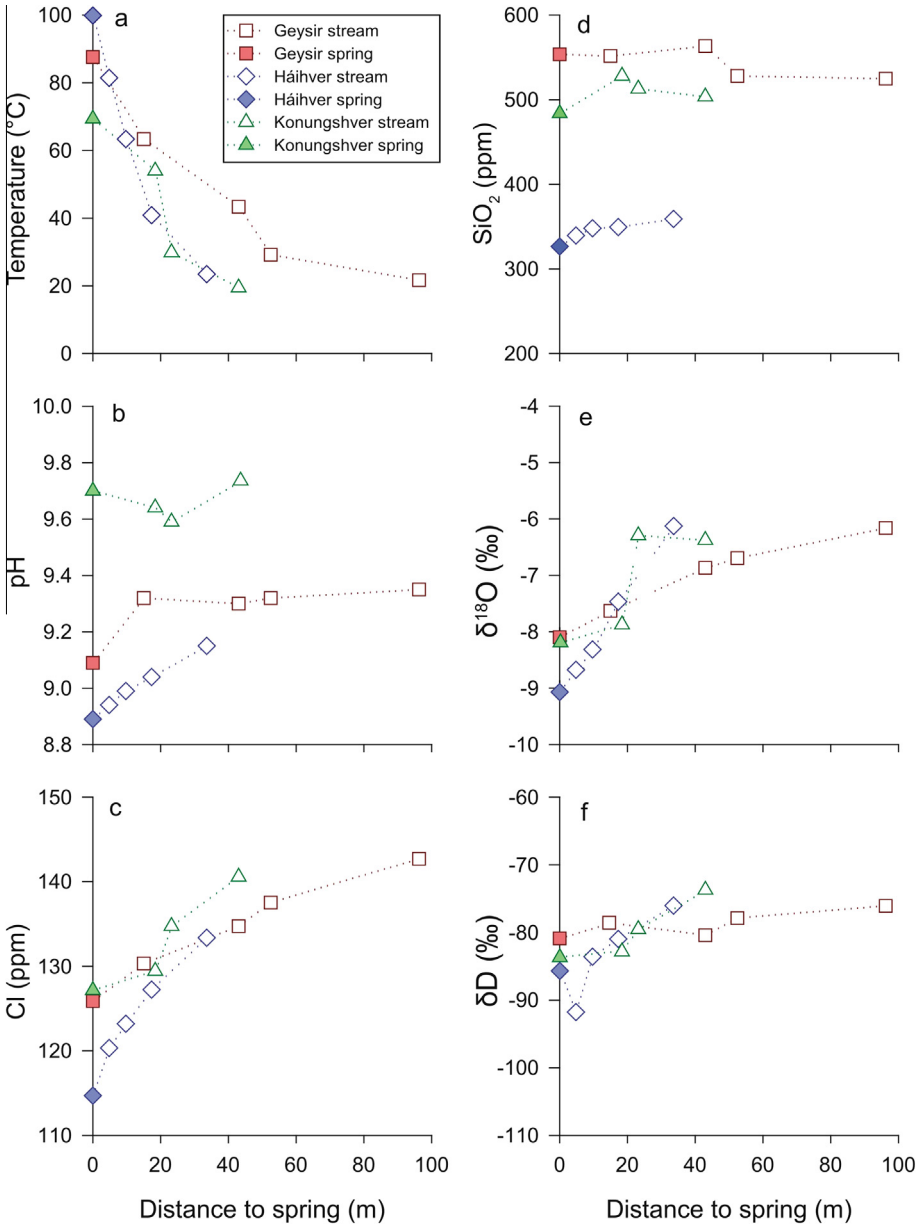

Fig. 3. Variation diagrams indicating downstream trends for (a) temperature, (b) pH, (c) chlorine concentrations, (d) SiO_2 concentrations, (e) $\delta^{18}O$ and (f) δD. Data for Konungshver site 12-Gey-15 not shown (see text).

lowermost part of the stream, an increasing amount of material of external origin in the deposit showed signs of advanced silicification, e.g., in the form of silicified leaves.

2.1.3. Konungshver

The Konungshver hot spring and outflow stream are situated on a small hill between the Geysir and Háihver streams. The pool had an irregular shape, with a maximum diameter of ~7 m. Bottom sediments were reddish brown in the inner part of the pool and formed a whitish siliceous crust at the <2 cm high rim (Fig. 2d). The hot spring temperatures varied between 70 °C in the center and 67 °C at the rim of the pool.

Two outflow channels discharged in the same sector and merged into one stream downhill. The main outflow channel was about 5 cm deep and 15 cm wide. The water flowed down a wide area with a gentle slope at an average velocity of ~1 m s^{-1}. The surface was dominated by reddish, brownish siliceous crust and ooze. Stream water temperatures decreased to 16 °C over a distance of ~20 m (Fig. 3a), while the pH varied between 9.6 and 9.8 (as measured at 20 °C) (Fig. 3b).

The silica precipitate appeared as whitish and brownish thin crust and ooze. The siliceous sinter deposits consisted of brownish, irregular laminae with pores and knobs that were intercalated with purer, homogeneous, and denser

gray layers. Brownish deposits locally comprised small areas with palisades. A homogeneous gray-brown, dense crust covered the irregular layers and cavities at the water-sediment interface. The brownish laminae were ⩽10 mm thick, whereas the pure laminae were not more than ~2 mm thick.

3. METHODS

3.1. Sampling strategy and analytical procedures

Sampling was conducted in June 2012. Five sampling sites were selected at each of the three systems, starting at the hot spring and subsequently at roughly regular intervals downstream, over distances imposed by the temperature gradient and local conditions. The most distant site in the Geysir trajectory was not examined for silicon isotopes, because the stream water may have been affected by mixing with input from a nearby stream. Stream flow rates were estimated by measuring the velocity of a floating object.

Water samples were collected in duplicate for determining the concentrations of major cations and anions, as well as the stable isotope ratios of hydrogen, oxygen and silicon. At each site, the pH, temperature and H_2S content of the water were measured in situ, using a standard multimeter and Hg-acetate titration (Arnórsson et al., 2006). Samples for major element analysis were filtered through 0.2 μm cellulose acetate filters into HDPE bottles. Aliquots for cation determinations (B, Si, Na, K, Ca, Mg, Fe, Al) were acidified with 1% HNO_3 (Suprapur®, Merck) and were analyzed by ICP-OES (Spectro-Ciros) at the University of Iceland. Aliquots for anion determinations (F, Cl, CO_2, SO_4) were not treated further and were analyzed by ion chromatography (IC) at the University of Iceland. Quality of analytical data was determined by repeated analysis of geothermal standard water (SPEX CertPrep) and duplicate sample measurements. Based on these measurements, the measurement uncertainty (as defined by Potts, 2012) for the ICP-OES and IC is between 1–10%, and less than 3% for most elements. Charge imbalance calculated using the PHREEQC program (Parkhurst and Appelo, 1999) with phreeqc.dat database at the temperature of pH measurement was on average 0.7% with maximum and minimum of −2.3 to 4.8%. For comparison and to check for possible silica polymerization upon sample storage, silica concentrations were also analyzed by spectrophotometer (Shimadzu UV-1800) at Utrecht University, using a modified molybdate blue method (Iler, 1979). Analytical quality was verified by repeated analyses of a Si standard solution (1000 mg/l Si Merck Certipur®) and analytical precision was on average 5%.

Samples for oxygen and hydrogen isotope analysis were collected in amber-glass bottles that were sealed with air-tight lids and analyzed using a Gas Bench coupled to a Thermo Delta plus and a Finnigan MAT253 mass spectrometer, respectively (Nelson, 2000), both at Utrecht University. Based on repeated measurements of in-house standards and SMOW-SLAP, the measurement uncertainty (as defined by Potts, 2012) was 0.3‰ for oxygen and 6‰ for hydrogen measurements.

Water samples for silicon isotope analysis were sampled in duplicate and filtered on site using disposable 0.2 μm nylon filters into HDPE bottles, and were immediately diluted ~5× with ultra-pure water to inhibit precipitation of silica upon sample storage.

Samples of solid silica were collected in duplicate by sampling the uppermost layer (<0.2 cm) of submerged deposits, which was in direct contact with the water of the pool or stream. Samples of silica sinter were analyzed by X-ray diffraction at Utrecht University using CoK_α radiation to determine the dominant mineral phase. The analysis of the major elements was carried out at Utrecht University. The samples were digested in HF/HNO_3 mixture (4:1), dried down and taken up in 2% HNO_3. This sample solution was measured by ICP-OES (Varian 730-ES). Silicon concentrations were determined on the same $NaOH{\cdot}H_2O$-digested samples that were prepared for the silicon isotope analyses and measured by ICP-OES (Varian 720-ES, VU University, Amsterdam). The measurement uncertainty for both optical ICP-OES systems, based on the measurement of certified reference materials (BHVO-2 and BCR-2), was <4%.

3.2. Silicon isotope analysis

The silicon isotope analyses of silica crusts and water samples were conducted at VU University, Amsterdam, using a method described by Van den Boorn et al. (2006). Small slivers of silica crusts (~0.5 mg) were mixed with sodium hydroxide monohydrate ($NaOH{\cdot}H_2O$) and placed into a Parr bomb at 200 °C for two nights. Multiple digestion steps were applied if necessary, where the residual solid was separated from the supernatant. The resulting solutions were purified using a cation exchange resin (Biorad AG50-X8). To test for possible loss of silica during purification, silica concentrations were re-measured by ICP-OES. Only yields >97% were considered acceptable.

A disadvantage of the purification technique of Van den Boorn et al. (2006) for water samples could be that the resin does not retain anions such as sulfate and fluoride. Van den Boorn et al. (2009) reported that the presence of sulfate in the measurement solution can induce shifts in the silicon isotope results of MC-ICPMS analyses. The SO_4/Si mass ratios of our water samples (0.3–0.9) could result in a shift of δ^{30}Si of more than 1.5‰ according to the findings of these authors (their Fig. 1). In order to remove sulfate and fluoride through precipitation of insoluble $BaSO_4$ and BaF, we treated 1 ml of the sample solution with 0.3 ml of a 1000 ppm Ba solution, before the sample was loaded onto the column. The silicon and sulfate yields of the precipitation step and the column extraction were tested by ICP-OES. The silicon yield was better than 90%, whereas the sulfate concentrations in the measurement solution were below detection limit (<0.3 ppm). Potential cation impurities were below practical ICP-OES detection limits as well.

Silicon isotope analyses of the solid and water samples were conducted with a ThermoFinnigan Neptune

MC-ICPMS. Sample introduction was done with a Cetac Aridus 1 desolvating nebulizer (solid samples) or with a quartz spraychamber (water samples). The ^{28}Si blank levels were $\leqslant$80 mV, with typical concentrations for standards and samples of 1 ppm which yielded ^{28}Si intensities of 6 to 8 V. The ^{28}Si procedural blank is $\leqslant$0.8 μg, which is about 0.7% of the total amount of silicon processed. Data were collected in static mode at medium resolution ($R_p = 8000$), with ^{28}Si in faraday cup L4, ^{29}Si in L1 and ^{30}Si in the central cup. The sample standard bracketing technique was applied, taking possible instrumental mass discrimination into consideration. Silicon isotope data are reported in the delta notation (in ‰) relative to NIST RM8546 (NBS-28):

$$\delta^{29}Si = \frac{(^{29}Si/^{28}Si)_{sample}}{(^{29}Si/^{28}Si)^{0.5}_{std-I} \cdot (^{29}Si/^{28}Si)^{0.5}_{std-II}} - 1 \quad (1)$$

$$\delta^{30}Si = \frac{(^{30}Si/^{28}Si)_{sample}}{(^{30}Si/^{28}Si)^{0.5}_{std-I} \cdot (^{30}Si/^{28}Si)^{0.5}_{std-II}} - 1 \quad (2)$$

The abbreviations std-I and std-II refer to the standards measured before and after each sample, respectively. The bracketing standard NBS-28 was prepared in the same way as the reference materials and solid samples (following Van den Boorn et al., 2006), with silica recovery yields >97% as adopted requirement for analysis. Each sample was measured twice, except when results for duplicate samples (taken at the same sample location) differed less than 0.5‰, i.e. two times the analytical precision. The difference for duplicate samples was usually less than 0.5‰, in most cases (73%) less than 0.4‰. Data processing was conducted offline following the data rejection criteria of Van den Boorn et al. (2006). Only results that fulfilled all criteria (concerning mass bias, blank contribution and internal precision) were accepted.

The precision of $\delta^{30}Si$ was $\leqslant$0.22‰ (2 s.d.), based on repeated measurements of international standards BHVO-2 (aliquot 1: average $\delta^{30}Si = -0.32 \pm 0.15$‰; 2 s.d., $n = 3$; aliquot 2: average $\delta^{30}Si = -0.39 \pm 0.21$‰; 2 s.d., $n = 3$) and AGV-2 (aliquot 1: average $\delta^{30}Si = -0.13 \pm 0.22$‰; 2 s.d., $n = 3$; aliquot 2: average $\delta^{30}Si = -0.01$, $n = 2$, where 'aliquot' refers to a quantity that underwent the complete digestion and purification procedure (without the Ba treatment step for S and F removal), and n refers to the number of repeated analyses on the MC-ICPMS). The accuracy of the measurements can be inferred from the BHVO-2 standard. Reported literature values e.g., by Zambardi and Poitrasson (2011) yield $\delta^{30}Si$ values of -0.27 ± 0.08‰ and thus agree well with the obtained $\delta^{30}Si$ value of this study (see above; measured in a 6 month time scale). Measurements of two in-house standards (Silicon Single Crystal (SSC) and CPI) yielded for the SSC an average $\delta^{30}Si$ of -2.59 ± 0.14‰ (aliquot 1, 2 s.d., $n = 5$) and -2.57 ± 0.12‰ (aliquot 2, 2 s.d., $n = 4$). The CPI in-house standard gave $\delta^{30}Si$ of -0.47 ± 0.17‰ (2 s.d.). This value of the SSC agrees well with the data for this standard reported by Kempl et al. (2013). Based on the replicate runs of the in-house standards and certified reference materials, we estimate our measurement uncertainty for $\delta^{30}Si$ to be 0.23 at the 95% confidence level.

3.3. Geochemical calculations

Aqueous speciation and mineral saturation were calculated from the major elemental composition with the aid of PHREEQC using the wateq4f.dat database (Parkhurst and Appelo, 1999). The calculations are based on the amorphous silica saturation state according to the reaction.

$$SiO_{2\ am.silica} + 2H_2O \leftrightarrow H_4SiO_4 \quad (3)$$

using the solubility data reported by Gunnarsson and Arnórsson (2000),

$$\log K = -8.476 - 485.24T^{-1} - 2.268 \times 10^{-6}T^2 + 3.068 \log T \quad (4)$$

Precipitation rates were calculated following Rimstidt and Barnes (1980). The scheme is based on reaction 3, which describes the precipitation and dissolution of amorphous silica as a dehydration and hydration process, respectively. Assuming an unlimited amount of water with dissolved H_4SiO_4 and a reaction rate proportional to the interfacial area (A) and inversely proportional to the mass of water (M), and taking the activity of pure substances to be unity and the activity coefficients of uncharged species to be one, the rate of silica precipitation (ppt) is expressed by:

$$\text{rate(ppt)} = \frac{\delta m H_4SiO_4}{\delta t} = k(A/M)(1 - Q/K) \quad (5)$$

where Q and K are the activity product and equilibrium constant, respectively, mH_4SiO_4 is the silicic acid concentration in molal, t the time in seconds and k is the rate constant, which depends on the temperature according to:

$$\log k = -0.369 - 7.890 \times 10^{-4}T - 3438/T \quad (6)$$

Using the above relations, the rate of amorphous silica precipitation can be assessed for a given A/M ratio. For the investigated streams, this extent (A/M) was approximated from field conditions by assuming a flat open stream channel with a uniform water depth, no borders (because of the shallow water depths relative to the surface areas) and a constant specific volume of water (i.e. independent of the temperature variations). For 1 cm of water depth, the A/M ratio will be 0.1 if units are expressed in meters and kg.

4. RESULTS

4.1. Water chemistry

Major element concentrations and $\delta^{18}O$ and δD in the water samples are reported in Table 1. These samples are characterized by alkaline pH values and temperatures between 20 and 100 °C. The most abundant components are Si, Na, K, CO_2, Cl and SO_4.

The outflow streams showed distinct trends downstream (Fig. 3). The concentrations of Cl, SO_4, CO_2 and Na increased, whereas Al, Ca and H_2S concentrations tended to decrease. The pH in the Geysir outflow stream remained relatively constant at ~9.3, whereas the Háihver and Konungshver streams showed a slight increase from 8.9 to 9.2 and 9.6 to 9.8, respectively (Fig. 3b). In contrast, the SiO_2 concentrations were relatively stable over the

Table 1
Chemical composition of geothermal hot spring water and discharge streams. *Data from this site are not included in discussions because of anomalous aqueous concentrations of SiO_2 and other cations and a deviating Si isotope composition of stream-bed silica.

Sample no	Location	Location and m down stream	t °C	pH/ °C	SiO_2 [a] ppm	SiO_2 [b] ppm	B ppm	Na ppm	K ppm	Ca ppm	Mg ppm	Fe ppm	Al ppm	Cl ppm	F ppm	SO_4 ppm	CO_2 ppm	H_2S ppm	$\delta^{18}O$ ‰	δD ‰	Ib[c] %
12-GEY-01	Geysir spring	64°18′49.29″ 20°17′58.54″	90	9.09/31	554	501	1.19	258	30.7	0.86	0.016	<0.01	0.57	126	8.21	96.3	121	1.02	−8.1	−81	4.8
12-GEY-02	Geysir downstream 1	15	64	9.32/20	552	539	1.14	249	27.3	0.83	<0.004	<0.01	0.65	130	8.68	102	123	0.17	−7.6	−79	0.2
12-GEY-03	Geysir downstream 2	43	40	9.30/24	563	539	1.19	260	28.2	0.85	<0.004	<0.01	0.65	135	8.98	106	121	<0.03	−6.9	−80	0.6
12-GEY-04	Geysir downstream 3	52	20	9.32/22	528	533	1.15	257	24.5	0.78	<0.004	<0.01	0.63	138	9.20	108	127	<0.03	−6.7	−78	−0.8
12-GEY-05	Geysir downstream 4	96	22	9.35/19	525	522	1.22	268	24.5	0.77	<0.004	<0.01	0.66	143	9.54	113	138	<0.03	−6.2	−76	−0.7
12-GEY-06	Háihver spring	64°18′50.01″ 20°18′21.98″	100	8.89/23	327	335	0.98	234	8.6	0.96	<0.004	<0.01	0.25	115	16.0	82.7	147	1.29	−9.1	−86	2.4
12-GEY-07	Háihver downstream 1	5	81	8.94/28	340	368	1.01	242	8.8	1.06	0.004	<0.01	0.47	120	16.6	89.9	146	0.26	−8.7	−92	1.4
12-GEY-08	Háihver downstream 2	10	65	8.99/24	348	360	1.02	247	8.7	1.10	0.008	<0.01	0.47	123	17.0	93.6	147	0.05	−8.3	−84	1.3
12-GEY-09	Háihver downstream 3	17	41	9.04/25	350	375	1.09	262	9.4	1.15	0.018	<0.01	0.47	127	17.5	96.8	149	<0.03	−7.5	−81	2.5
12-GEY-10	Háihver downstream 4	34	23	9.15/21	359	362	1.11	262	9.4	1.05	0.019	<0.01	0.44	133	18.3	99.0	152	<0.03	−6.1	−76	0.3
12-GEY-11	Konungshver spring	64°18′49.62″ 20°18′06.56″	67	9.70/18	484	487	1.07	241	19.1	0.76	<0.004	<0.01	0.21	127	8.71	107	59.1	0.45	−8.2	−84	−0.9
12-GEY-12	Konungshver downstream 1	18	54	9.64/22	528	498	1.16	257	23.3	0.82	<0.004	<0.01	0.28	129	8.89	112	64.0	0.08	−7.9	−83	0.0
12-GEY-13	Konungshver downstream 2	23	30	9.59/25	513	509	1.19	261	22.2	0.79	<0.004	<0.01	0.25	135	9.23	117	66.5	<0.03	−6.3	−80	−0.3
12-GEY-14	Konungshver downstream 3	43	19	9.73/16	504	493	1.25	276	22.0	0.70	<0.004	<0.01	0.26	141	9.62	122	79.5	<0.03	−6.4	−74	−0.2
12-GEY-15*	Konungshver downstream 4	48	16	9.78/15	292	288	1.19	263	23.9	0.36	0.020	<0.01	0.12	145	9.88	126	102	<0.03	−6.2	−71	−0.7

[a] Total SiO_2 determined by ICP-OES.
[b] Mono-, di-, trimeric silica determined by spectrophotometer.
[c] Percentage ion balance at the temperature of pH measurement calculated with the PHREEQC program using the wateq4f.dat database.

investigated stream intervals (Fig. 3d). An exception was a strong drop of SiO_2 concentration at the most distant sampling site in the Konungshver stream (12-Gey-15). The anomalous low concentration of aqueous SiO_2 and several other cations (Table 1) and a deviating $\delta^{30}Si$ value for the stream-bed sinter with a poor reproducibility of results for duplicate samples, question the representativeness of data from this site, and we will therefore not include it in further discussions.

The $\delta^{18}O$ and δD values for the Geysir spring were −8.1‰ and −81‰, for the Háihver spring −9.1‰ and −86‰, and for the Konungshver spring −8.2‰ and −84‰, respectively (Table 1). These results are consistent with data reported earlier for the Geysir field (Arnórsson, 1985). The $\delta^{18}O$ and δD values of the stream waters were less negative than the pool waters (Fig. 3e, f).

4.2. Sinter mineralogy and chemistry

The chemical compositions of the sinter deposits are presented in Table 2. The sinters predominantly consisted of silica, with SiO_2 concentrations of ⩾97 wt%, except for the deposit in the Háihver spring (92 wt%). Other constituents including Al_2O_3, CaO, FeO and Na_2O were detected in minor amounts. Sinters from the springs contained less SiO_2 and more Al_2O_3 (up to 3.2 wt%), FeO (up to 2.4 wt%), CaO and Na_2O than the deposits in the stream beds. The concentration of minor elements tended to decrease downstream, e.g., for Al_2O_3 from 0.3 to 0.02 wt% at Geysir, 3.2 to 0.8 wt% at Háihver, and 1.1 to 0.2 wt% at Konungshver, except for the second to last sampling point where concentrations were relatively high. According to XRD analysis, all siliceous sinter samples were composed of opal-A.

4.3. Silicon isotopes

The silicon isotope values ($\delta^{29}Si$ and $\delta^{30}Si$) in water and sinter samples are given in Table 3. Dissolved silica in the hot springs and outflow stream waters ranged in $\delta^{30}Si$ values from 0.0‰ to 0.5‰ (Fig. 4). They are close to the average value around +0.2‰ reported for hot springs in the Yellowstone and Mammoth geothermal areas (USA) (Douthitt, 1982) and values of ca. −0.3‰ of deep-sea hydrothermal waters (De La Rocha et al., 2000). Available results for other Icelandic thermal waters vary between $+0.51 \pm 0.12$‰ for hot springs near Lake Myvatn (Opfergelt et al., 2011) and −0.20‰ for a hot spring sample from Deildartunguhver (Opfergelt et al., 2013). In general, $\delta^{30}Si$ values of the stream waters remained relatively constant along the sampled stretches. Only the lower sample points of Háihver and Konungshver showed a slight increase of 0.4‰ and 0.3‰, respectively. The $\delta^{30}Si$ differences between duplicate samples was ⩽0.4‰.

Silicon isotope compositions of the sinter deposits displayed relative enrichment in ^{28}Si and distinct downstream trends with negative $\delta^{30}Si$ values decreasing with distance away from the spring (Fig. 4). Samples of the spring deposits had lowest $\delta^{30}Si$ values at Geysir (−1.9‰), intermediate at Háihver (−0.8‰), and highest at Konungshver (−0.1‰). The $\delta^{30}Si$ values for the stream-bed sinters ranged between −1.3‰ and −3.0‰ at Geysir, between −0.6‰ and −4.0‰ at Háihver, and between −1.6‰ and −3.2‰ at Konungshver. Repeatability of duplicate samples was ⩽1.3‰ ($\delta^{30}Si$ difference), and in ca. 50% of the cases ⩽0.5‰. Our results fall in the range of hot spring sinters reported in previous studies, which comprises $\delta^{30}Si$ values between +0.9‰ and −3.1‰ for geyserites, opaline sinter, chalcedony and silicified plants (Douthitt, 1982; Ding et al., 1996).

5. DISCUSSION

5.1. Processes controlling amorphous silica precipitation

Although silica deposition is commonly associated with cooling, the factors that govern precipitation from

Table 2
Compositions of opal-A sinters from spring pools and streambeds.

Sample no	Location	SiO_2 wt%	Al_2O_3 wt%	CaO wt%	FeO wt%	K_2O wt%	MgO wt%	MnO wt%	Na_2O wt%	P_2O_5 wt%	SO_3 wt%	TiO_2 wt%
12-GEY-01	Geysir spring	99.03	0.26	0.17	0.088	0.097	0.051	0.003	0.28	<d.l.	<d.l.	0.017
12-GEY-02	Geysir downstream 1	99.67	0.16	0.037	0.004	0.044	0.002	0.0003	0.080	<d.l.	<d.l.	0.001
12-GEY-03	Geysir downstream 2	99.79	0.014	0.054	<d.l.	0.039	0.002	0.0005	0.10	<d.l.	<d.l.	0.001
12-GEY-04	Geysir downstream 3	99.74	0.021	0.058	0.012	0.045	0.007	0.001	0.12	<d.l.	<d.l.	0.003
12-GEY-05	Geysir downstream 4	n.a.	n.a.	n.a.	n.a.	n.a.	n.a.	n.a.	n.a.	n.a.	n.a.	n.a.
12-GEY-06	Háihver spring	92.13	3.2	0.97	2.4	0.16	0.000	0.038	0.52	0.040	0.051	0.50
12-GEY-07	Háihver downstream 1	96.97	1.6	0.45	0.24	0.19	0.074	0.005	0.45	<d.l.	<d.l.	0.047
12-GEY-08	Háihver downstream 2	98.97	0.47	0.10	0.19	0.043	0.046	0.004	0.13	0.005	<d.l.	0.039
12-GEY-09	Háihver downstream 3	99.66	0.12	0.037	0.059	0.016	0.013	0.002	0.071	<d.l.	<d.l.	0.012
12-GEY-10	Háihver downstream 4	99.68	0.077	0.054	0.060	0.016	0.017	0.002	0.080	0.003	<d.l.	0.011
12-GEY-11	Konungshver spring	97.10	1.1	0.19	0.40	0.23	0.15	0.007	0.67	<d.l.	0.068	0.065
12-GEY-12	Konungshver downstream 1	98.82	0.37	0.20	0.20	0.080	0.079	0.004	0.19	<d.l.	<d.l.	0.040
12-GEY-13	Konungshver downstream 2	99.28	0.16	0.13	0.10	0.071	0.041	0.002	0.19	<d.l.	<d.l.	0.017
12-GEY-14	Konungshver downstream 3	98.21	0.50	0.25	0.38	0.12	0.16	0.006	0.30	<d.l.	<d.l.	0.065
12-GEY-15*	Konungshver downstream 4	99.33	0.15	0.10	0.099	0.066	0.053	0.002	0.18	<d.l.	<d.l.	0.016

<d.l. = below detection limit, n.a. = not analyzed.
* Data from this site are not included in discussions (see text).

Table 3
Silicon isotope composition for spring and stream waters and for opal-A sinters from spring pools and stream beds. No standard deviation is reported for two measurements.

Location	Water phase								Solid phase (amorphous silica)							
	Sample no. water phase	n[a]	$\delta^{30}Si$ ‰	Average $\delta^{30}Si$ ‰	1 sd ‰	$\delta^{29}Si$ ‰	Average $\delta^{29}Si$ ‰	1 sd ‰	Sample No. Solid phase	n[a]	$\delta^{30}Si$ ‰	Average $\delta^{30}Si$ ‰	1 sd ‰	$\delta^{29}Si$ ‰	Average $\delta^{29}Si$ ‰	1 sd ‰
Geysir spring	12-Gey-01-1	4	0.13	0.20	± 0.06	0.01	0.05	± 0.05	12-Gey-01-1	5	−1.26	−1.89	± 0.64	−0.66	−0.94	± 0.28
			0.20			0.06					−1.14			−0.63		
	12-Gey-01-2		0.18			0.01			12-Gey-01-2		−2.20			−0.98		
			0.28			0.12					−2.45			−1.26		
											−2.41			−1.16		
Geysir downstream 1	12-Gey-02-1	4	−0.02	0.01	± 0.23	−0.11	−0.05	± 0.08	12-Gey-02-1	2	−1.03	−1.31		−0.46	−0.59	
			0.16			−0.04										
	12-Gey-02-2		0.19			0.06			12-Gey-02-2		−1.59			−0.73		
			−0.30			−0.11										
Geysir downstream 2	12-Gey-03-1	4	0.07	0.03	± 0.08	−0.07	−0.02	± 0.04	12-Gey-03-1	5	−2.51	−3.13	± 0.66	−1.28	−1.63	± 0.31
			−0.05			−0.02					−-2.37			−1.37		
	12-Gey-03-2		0.13			0.03			12-Gey-03-2		−3.30			−1.65		
			−0.03			−0.01					−3.77			−1.97		
											−3.68			−1.89		
Geysir downstream 3	12-Gey-04-1	4	0.16	0.15	± 0.17	0.08	0.08	± 0.05	12-Gey-04-1	4	−3.28	−2.91	± 0.78	−1.68	−1.48	± 0.36
			0.39			0.15					−3.82			−1.88		
	12-Gey-04-2		0.01			0.04			12-Gey-04-2		−2.31			−1.21		
			0.05			0.04					−2.22			−1.14		
Geysir downstream 4	12-Gey-05-1								12-Gey-05-1							
	12-Gey-05-2								12-Gey-05-2							
Háihver spring	12-Gey-06-1	4	0.23	0.13	± 0.25	0.01	−0.01	± 0.06	12-Gey-06-1	4	−0.43	−0.85	± 0.37	−0.26	−0.44	± 0.16
			−0.01			0.03					−0.70			−0.41		
	12-Gey-06-2		0.44			0.01			12-Gey-06-2		−0.98			−0.44		
			−0.12			−0.09					−1.29			−0.64		
Háihver downstream 1	12-Gey-07-1	4	0.25	0.07	± 0.23	0.01	−0.02	± 0.08	12-Gey-07-1	2	−0.61	−0.62		−0.28	−0.30	
			−0.26			−0.11										
	12-Gey-07-2		0.21			0.07			12-Gey-07-2		−0.63			−0.32		
			0.08			−0.04										
Háihver downstream 2	12-Gey-08-1	4	0.13	0.17	± 0.21	0.01	−0.03	± 0.04	12-Gey-08-1	2	−0.88	−0.85		−0.39	−0.39	
			−0.01			−0.04										
	12-Gey-08-2		0.48			0.00			12-Gey-08-2		−0.82			−0.38		
			0.10			−0.07										

Háihver downstream 3	12-Gey-09-1	4	0.17	0.15	± 0.22	0.04	0.01	± 0.05	12-Gey-09-1	2	−1.67	−1.55		−0.86	−0.78	
			−0.07			−0.06										
	12-Gey-09-2		0.44			0.06			12-Gey-09-2		−1.43			−0.70		
			0.05			0.01										
Háihver downstream 4	12-Gey-10-1	3	0.52	0.46	± 0.11	0.13	0.13	± 0.01	12-Gey-10-1	2	−4.20	−3.98		−2.19	−2.08	
			0.52			0.14										
	12-Gey-10-2		0.34			0.11			12-Gey-10-2		−3.76			−1.97		
Konungshver spring	12-Gey-11-1	4	0.28	0.23	± 0.03	0.07	0.04	± 0.05	12-Gey-11-1	2	−0.14	−0.09		−0.07	−0.02	
			0.22			0.06										
	12-Gey-11-2		0.21			0.06			12-Gey-11-2		−0.03			0.04		
			0.21			−0.03										
Konungshver downstream 1	12-Gey-12-1	4	0.12	0.21	± 0.18	−0.03	0.01	± 0.05	12-Gey-12-1	2	−1.46	−1.57		−0.65	−0.77	
			0.05			0.00										
	12-Gey-12-2		0.21			0.00			12-Gey-12-2		−1.68			−0.88		
			0.46			0.08										
Konungshver downstream 2	12-Gey-13-1	4	0.04	0.10	± 0.09	0.00	−0.01	± 0.04	12-Gey-13-1	2	−2.23	−2.57		−1.15	−1.33	
			0.00			−0.06										
	12-Gey-13-2		0.15			0.03			12-Gey-13-2		−2.91			−1.51		
			0.21			0.01										
Konungshver downstream 3	12-Gey-14-1	4	0.30	0.46	± 0.20	0.12	0.15	± 0.04	12-Gey-14-1	2	−2.98	−3.16		−1.51	−1.64	
			0.27			0.11					−3.34			−1.78		
	12-Gey-14-2		0.67			0.18			12-Gey-14-2		/			/		
			0.59			0.20										
Konungshver downstream 4	12-Gey-15-1*	5	1.19	1.08	± 0.54	0.41	0.37	± 0.11	12-Gey-15-1*	4	−1.20	−1.73	± 0.50	−0.61	−0.90	± 0.28
			0.49			0.23					−1.45			−0.75		
	12-Gey-15-2*		0.55			0.28			12-Gey-15-2*		−1.96			−0.97		
			1.46			0.49					−2.30			−1.26		
			1.70			0.45										

[a] Total number of measurements.

[*] Data from this site are not included in discussions because of anomalous aqueous SiO_2 concentration and Si isotope composition of stream-bed silica.

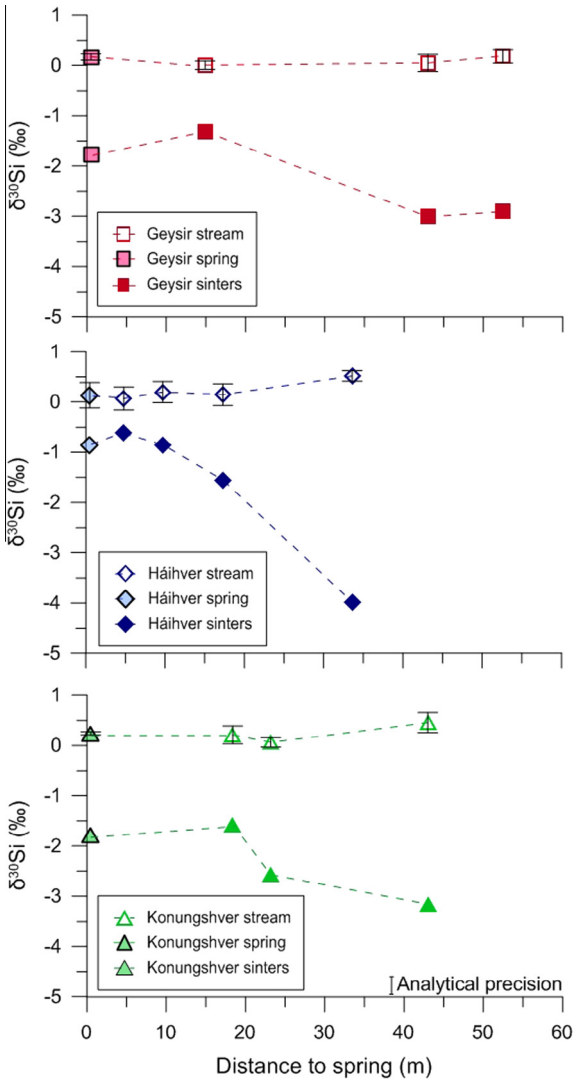

Fig. 4. Silicon isotope trends in sinter deposits and co-existing spring or stream water for Geysir (upper panel), Háihver (middle panel) and Konungshver (lower panel; stream and sinter data for site 12-Gey-15 not shown, see text). Error bars indicate 1 s.d. between replicate measurements. No error bars are shown for the sinters (see text and Table 3).

saturated hot spring waters remain under discussion (e.g., White et al., 1956; Rimstidt and Barnes, 1980; Guidry and Chafetz, 2002, 2003a; Jones and Renaut, 2003; Renaut and Jones, 2003; Rodgers et al., 2004; Icopini et al., 2005; Lynne et al., 2008; Lynne, 2012; Tobler et al., 2008; Tobler and Benning, 2013). In absence of evidence for a strong biological component, abiotic factors like rapid cooling and evaporative concentration appear to be dominant, but pH changes and cation effects could play a role as well (Iler, 1979; Carroll et al., 1998; Guidry and Chafetz, 2002; Mountain et al., 2003; Icopini et al., 2005; Tobler et al., 2008).

To explore potential controls on silica precipitation, elemental concentrations were compared with the amorphous silica saturation state (Fig. 5). Strong inverse correlations with temperature were observed, implying downstream increases in the saturation index. Moreover, positive correlations between the saturation index and Cl concentration are present. The downstream increases in Cl are likely caused by water loss (White et al., 1956; Guidry and Chafetz, 2002). Relationships between the silica saturation state and other parameters such as pH, SiO_2, Al and Ca concentrations are less obvious. Only at Háihver, positive correlations with pH and dissolved SiO_2 are seen but the small ranges and absence of relationships for the other streams make a control of these parameters improbable. The solubility of amorphous silica may also be influenced by dissolved cations such as Al (Iler, 1979; Van Cappellen and Qiu, 1997; Carroll et al., 1998), but the low concentrations in the streams (Al and Fe <0.66 ppm) and lack of a distinct relationship with amorphous silica saturation make significant effects from these elements equally unlikely. Similarly, calcite precipitation could suppress amorphous silica precipitation (Kastner et al., 1977), but the poor correlation between Ca concentrations and amorphous silica saturation excludes this as an important factor. In conclusion, obvious relationships between the saturation index, temperature and Cl concentration suggest that cooling and evaporation are the main causes of silica precipitation.

5.2. Relative importance of evaporation and temperature for amorphous silica precipitation

Although it has been inferred that temperature plays an important role in silica precipitation (Guidry and Chafetz, 2002; Tobler et al., 2008) and despite the fact that the decrease in temperature of the outflow streams away from the hot springs drastically lowers the amorphous silica solubility, measured SiO_2 concentrations showed little changes with temperature downstream (Fig. 3). Evaporation leads to increased concentrations of non-volatiles and may therefore also increase the level of silica supersaturation and induce its precipitation. The systematic downstream trends in $\delta^{18}O$ and δD (Fig. 3) and the maximum enrichment of about 2‰ and 8‰, respectively, are typical for hot spring systems (e.g., Arnórsson, 1985; Chafetz and Lawrence, 1994; Kele et al., 2008, 2011). Deposition of amorphous silica cannot be responsible for these isotope shifts, as it will remove the relatively heavy isotopes from the water (Clayton et al., 1972; Knauth and Epstein, 1975, 1976). Instead, the positive relationship between $\delta^{18}O$ and δD values away from the Local Meteoric Water Line (LMWL, Fig. 6) can be attributed to a gradual loss of light oxygen and hydrogen isotopes due to evaporation (Craig, 1961; Chafetz and Lawrence, 1994). Arnórsson (1985) distinguished two groups of Geysir waters based on their $\delta^{18}O$ and δD signatures. One group corresponds to the samples of this study (Fig. 6), and was also interpreted as stream waters influenced by evaporation. The other group plots near the LMWL or slightly above it, and is considered to represent mixtures of regional geothermal waters and non-thermal waters either from the interior or of local origin (Arnórsson and Andrésdóttir, 1995).

The increases in concentrations of conservative elements such as Cl can be used to quantify the amount of

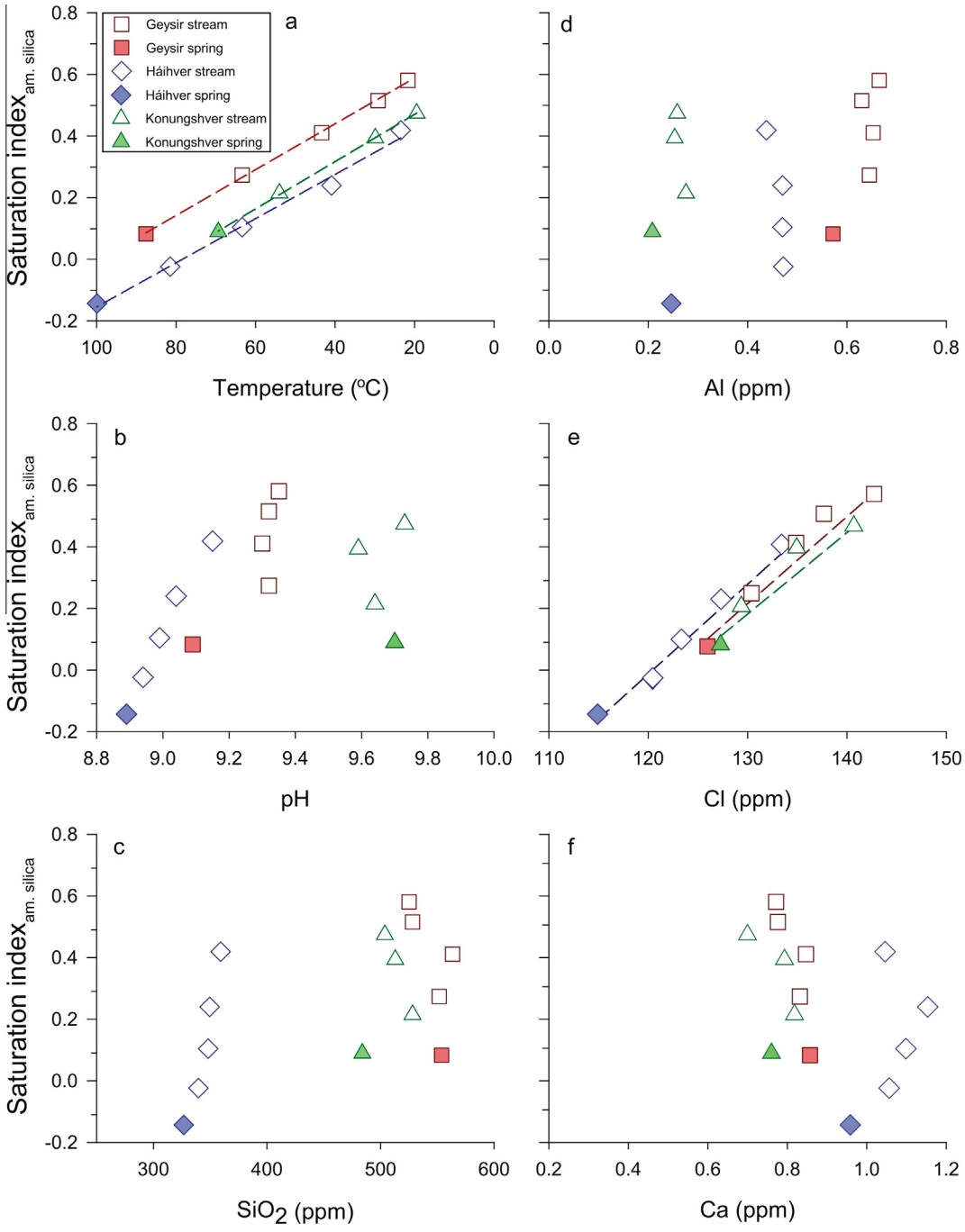

Fig. 5. Variation diagrams of the saturation index for amorphous silica against (a) temperature (correlation coefficients (c.c. $\geqslant$ 0.992), (b) pH (c.c. 0.02 (Konungshver) – 0.987 (Háihver)), (c) dissolved SiO_2 content (c.c. 0.101 (Konungshver) – 0.923 (Háihver)), (d) Al (c.c. 0.304 (Konungshver) – 0.655 (Geysir)), (e) Cl (c.c. $\geqslant$ 0.936), and (f) Ca (c.c. 0.208 (Konungshver) – 0.719 (Geysir). Filled symbols represent springs. Note that the saturation index correlates well with temperature and Cl content, which is taken as a proxy for the degree of evaporation (see text).

evaporation (e.g., White et al., 1956; Guidry and Chafetz, 2002). For the lowermost sampling points, the inferred water losses over total stream lengths due to evaporation are 12–14% (corresponding to ca. 0.3–1.1% loss per meter). The silica saturation indices should be affected accordingly. Fig. 7 shows the predicted silica concentrations in the solutions if no precipitation would have occurred (White et al., 1956), taking into account the calculated evaporative water losses. Differences with the measured SiO_2 concentrations represent the fractions of silica that must have precipitated.

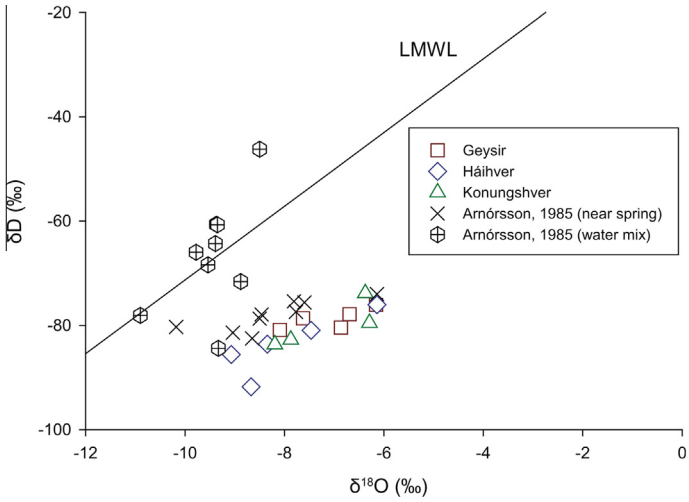

Fig. 6. Oxygen and hydrogen isotope diagram for the investigated spring and stream waters for Geysir, Háihver, and Konungshver (colored symbols) and for regional Geysir data (gray and black symbols) from Arnórsson (1985). Slopes of the individual trend lines are consistent with evaporation. The Local Meteoric Water Line (LMWL) is shown for comparison. (For interpretation of the references to color in this figure legend, the reader is referred to the web version of this article.)

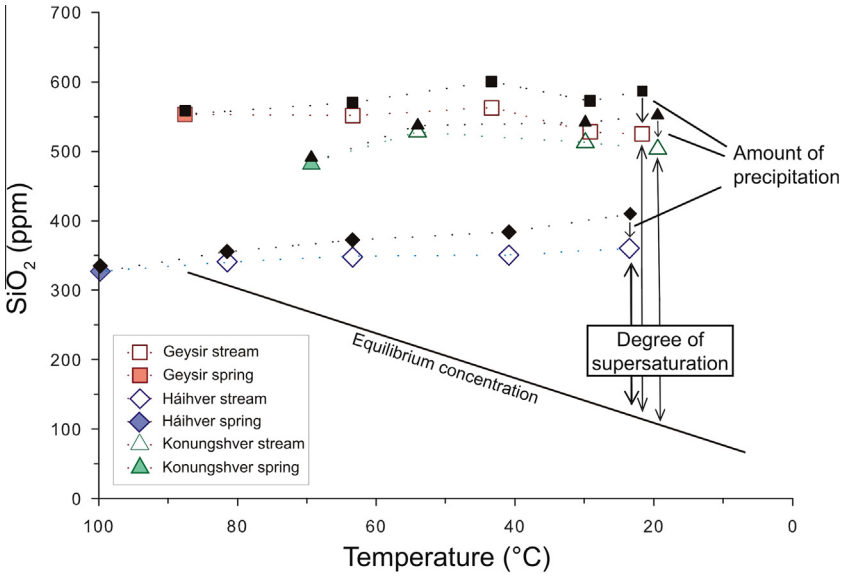

Fig. 7. Measured SiO_2 contents (open symbols) and predicted increases in SiO_2 (filled symbols) in response to evaporative water loss, assuming no silica precipitation for Geysir, Háihver, and Konungshver (dashed lines), compared with equilibrium concentration at saturation (black line) from Gunnarsson and Arnórsson (2000). Differences between predicted and measured SiO_2 concentration should represent the amount of precipitated siliceous sinter. Gap between equilibrium concentration and measured SiO_2 concentrations defines the degree of silica oversaturation.

Given the relatively stable SiO_2 concentrations in each stream, the differences tend to increase downstream, which implies increasing amounts of silica precipitation.

5.3. Silica precipitation and nucleation

Calculated precipitation rates (Eq. (5)) for amorphous silica in the streams range between 6.5×10^{-14} and 1.2×10^{-12} mol l^{-1} s^{-1} assuming $A/M = 0.1$ (Table 4). They increase with increasing temperature and decreasing saturation state (Fig. 8). This counterintuitive result is due to the temperature dependence of the reaction rate constant, which has a larger effect on the outcome than the saturation state does (e.g., Rimstidt and Barnes, 1980). Hence, the calculations predict that precipitation rates decrease downstream. Calculated precipitation rates are about three orders of magnitude slower than observed rates in field experiments in streams of the Geysir area, which yielded 0.2–1.4 kg yr^{-1} m^{-2} (Tobler et al., 2008), corresponding to a yearly increase in sinter thickness of 0.1–0.7 mm

Table 4
Calculated precipitation rates for amorphous silica in the streams, based on the scheme of Rimstidt and Barnes (1980).

Sample no.	Location	SiO_2 mol l^{-1}	T °C	k s^{-1}	K	Q/K	A/M	$Rate_{ppt}$ mol $l^{-1}s^{-1}$
12-GEY-01	Geysir spring	0.00923	88	6.5×10^{-11}	0.00535	1.7	0.1	4.7×10^{-12}
12-GEY-02	Geysir downstream 1	0.00919	63	1.4×10^{-11}	0.00378	2.4	0.1	2.0×10^{-12}
12-GEY-03	Geysir downstream 2	0.00939	43	3.3×10^{-12}	0.00272	3.5	0.1	8.0×10^{-13}
12-GEY-04	Geysir downstream 3	0.00880	20	4.6×10^{-13}	0.00174	5.0	0.1	1.9×10^{-13}
12-GEY-05	Geysir downstream 4	0.00875	22	5.4×10^{-13}	0.00181	4.8	0.1	2.1×10^{-13}
12-GEY-06	Háihver spring	0.00545	100	1.3×10^{-10}	0.00627	0.9	0.1	-1.7×10^{-12}
12-GEY-07	Háihver downstream 1	0.00566	82	4.5×10^{-11}	0.00492	1.1	0.1	6.7×10^{-13}
12-GEY-08	Háihver downstream 2	0.00580	63	1.4×10^{-11}	0.00378	1.5	0.1	7.5×10^{-13}
12-GEY-09	Háihver downstream 3	0.00583	41	2.7×10^{-12}	0.00260	2.2	0.1	3.3×10^{-13}
12-GEY-10	Háihver downstream 4	0.00599	24	6.3×10^{-13}	0.00187	3.2	0.1	1.4×10^{-13}
12-GEY-11	Konungshver spring	0.00807	69	2.1×10^{-11}	0.00414	1.9	0.1	2.0×10^{-12}
12-GEY-12	Konungshver downstream 1	0.00880	54	7.2×10^{-12}	0.00325	2.7	0.1	1.2×10^{-12}
12-GEY-13	Konungshver downstream 2	0.00855	30	1.1×10^{-12}	0.00212	4.0	0.1	3.3×10^{-13}
12-GEY-14	Konungshver downstream 3	0.00840	20	4.4×10^{-13}	0.00173	4.9	0.1	1.7×10^{-13}
12-GEY-15	Konungshver downstream 4	0.00487	16	3.2×10^{-13}	0.00160	3.0	0.1	6.5×10^{-14}

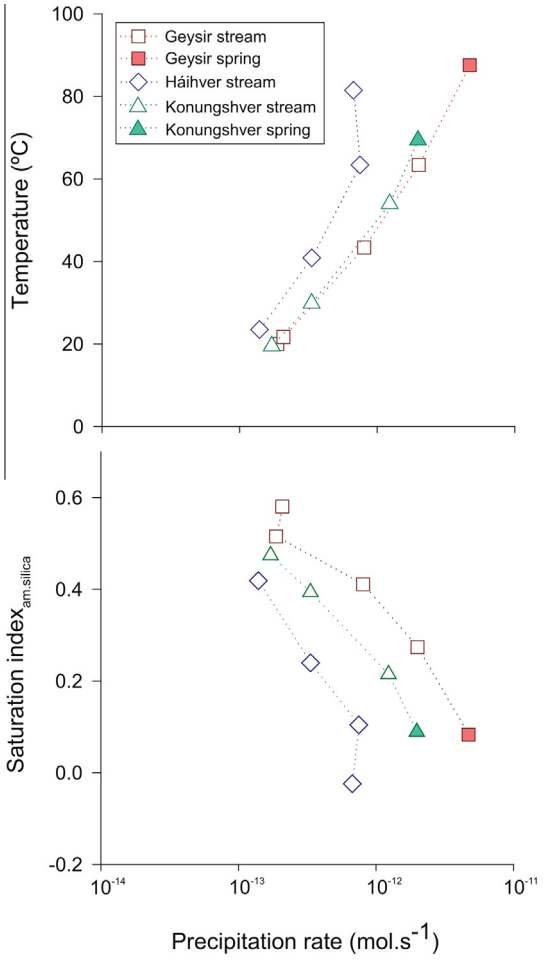

Fig. 8. Correlations between the silica precipitation rate, temperature and the saturation index for amorphous silica. Note that the precipitation rate shows a positive correlation with temperature and a negative correlation with the saturation state. The negative precipitation rate for Háihver pool reflects the undersaturated state of this water and is not shown in the figure.

(assuming a density of 2 g cm^{-3} for amorphous silica and zero porosity). It should be noted, however, that these results may not be directly comparable, given that precipitation in the experiments occurred largely at the air-water interface (presumably more driven by evaporation) rather than at the contact with the streambed. Also, significant discrepancies between calculated precipitation rates and field data are a common phenomenon, and may reflect a problem inherent to the theoretical approach (Rimstidt and Barnes, 1980; Renders et al., 1995; Carroll et al., 1998).

It is of interest to consider the possibility that silica deposition is not exclusively controlled by surface reactions but also by the nucleation, growth and aggregation of silica nanoparticles because these processes will have different effects on precipitation rate and Si isotope fractionation. Concentrations along the Geysir and Konungshver streams and at the last sampling point of the Háihver stream exceed the critical concentration for homogeneous nucleation (i.e. ca. 2.5× the equilibrium concentration; Weres et al., 1981). Furthermore, the induction time needed to form the first critical nuclei decreases downstream due to the increasing degree of supersaturation and decreasing temperature (Rothbaum and Rohde, 1979; Weres et al., 1981; Icopini et al., 2005). Hence, the high degrees of supersaturation would predict homogeneous nucleation in the water and deposition of pre-constituted particles (Campbell et al., 2001; Lynne and Campbell, 2004; Orange et al., 2013). Nevertheless, the closeness of ICP-OES and spectrophotometer results provide no evidence for significant polymerization in solution (Table 1). Presumably, homogeneous nucleation is hampered by delays in silica polymerization, as has been inferred for geothermal waters wherein polymerization is induced by fast cooling (Weres et al., 1981; Carroll et al., 1998; Tobler and Benning, 2013), and by relatively large ratios of streambed surface versus solution volume, favoring deposition on pre-existing surfaces. Furthermore, although microorganisms do not directly increase silicification kinetics (Konhauser et al., 2004), their presence highly influences the structure and fabric of silica deposits (Hinman and Lindstrom, 1996; Konhauser et al.,

2001; Handley et al., 2005; Jones and Renaut, 2010), and will thus have substantial effects on surface area and nucleation sites for abiotic precipitation.

5.4. Variations in silicon isotope compositions

5.4.1. $\delta^{30}Si$ in pool waters

The average δ^{30}Si value of +0.2‰ for the pool waters falls well within the range of −0.2‰ to +0.6‰ found for other hot springs so far (Douthitt, 1982; Ding et al., 1996; Opfergelt et al., 2011, 2013).

The pool waters are enriched in ^{30}Si relative to volcanic rocks from which the silicon is most likely derived (average δ^{30}Si for Icelandic lavas is ca. −0.3‰, Savage et al., 2011), which can be explained if precipitation occurs during water ascent. The temperature difference between the source aquifer of around 260 °C (Arnórsson, 1985; Kaasalainen and Stefánsson, 2012) and the surface discharge waters of ⩽100 °C may have induced precipitation of isotopically light silica in subsurface conduits, so that the hot spring waters have evolved to more positive δ^{30}Si values at the surface. The dynamic nature of the springs, due to convection, surging, boiling and evaporation (e.g., Braunstein and Lowe, 2001), creates different conditions for silica precipitation than in the streams, so that pool data will not be considered when we discuss controls of silicon isotope fractionation below.

5.4.2. $\delta^{30}Si$ in stream waters

The fairly homogeneous δ^{30}Si values of about +0.2‰ along the entire flow path of the stream waters (Fig. 4) can be explained as a reservoir effect. The δ^{30}Si signature of the flowing water reservoir is not measurably affected by the relatively small amounts of silica extracted during subaqueous precipitation. In contrast, the solid deposit is entirely composed of the precipitating phase, so that its downstream δ^{30}Si variability can be approximated as a result of effective fractionation with a continuously changing magnitude out of an isotopically uniform reservoir.

5.4.3. Representativity of $\delta^{30}Si$ variations in siliceous sinters

Silica precipitation in outflowing streams of hot springs may be influenced by seasonal variations in environmental conditions, as air temperature, rain or snowfall and presence of sunlight will affect the rate of cooling and evaporation, the pathway of opal-A precipitation, flow dynamics and microbial growth (e.g., Hinman and Lindstrom, 1996; Campbell et al., 2001; Konhauser et al., 2001; Channing and Butler, 2007; Tobler et al., 2008; Jones and Renaut, 2010). In a detailed study of the discharge apron of Geysir, Jones and Renaut (2010) concluded that various components of the siliceous sediment observed in pools are associated with seasonally influenced processes. The authors noted a potential for the formation of cyclic laminae, consisting of cryogenic, largely unconsolidated opal-A in winter times and harder, more cemented layers in the spring and summer months when expansion of microbial mats provides nucleation/precipitation sites for silica precipitation. Hence, although metabolic effects on silicification are probably minimal (Konhauser et al., 2004), microorganisms might influence silicon isotope fractionation through their role in fabric development of the sinters. The existence of (seasonally induced) vertical isotopic variability in sinter layers is therefore conceivable.

Because the sinter deposits were sampled from streambed stretches with flowing water and not from pools, and since their δ^{30}Si values systematically change downstream in each of the three systems and are similar at sampling points with corresponding water temperatures, it is reasonable to assume that isotopic compositions of the sampled top layer of the hard surfaces represent environmental conditions during the field survey and are not inherited from past deposition episodes. Only the relatively large differences in δ^{30}Si between some duplicate samples might be attributable to small-scale isotopic heterogeneity in the layered sinter crust, which is potentially associated with deposition under strongly different seasonal conditions. Hence, the large δ^{30}Si variations between −0.1‰ and −4.0‰ and the downstream trends are taken as contemporary features, suitable to evaluate isotopic fractionation using the simultaneously sampled stream waters. Thicknesses of the top layer that had been produced during the spring-summer season when sampling was undertaken were difficult to ascertain but the local presence of silicified microbial structures and biofilms suggests that they exceeded several millimeters.

5.5. Controls of silicon isotope fractionation

Because the δ^{30}Si signatures of water and solid are approximately similar for the three systems at a given temperature, we combined the data from the three streams to explore the potential controls of silicon isotope fractionation that are seemingly related to the degree of cooling. The difference between measured δ^{30}Si values for co-existing sinter and stream water, expressed as $\Delta^{30}Si_{solid-water}$ was taken to represent the magnitude of local (apparent) fractionation, and results from sampling points with roughly the same temperature (less than 5 °C difference) were averaged. As shown in Fig. 9, there is a conspicuous inverse relationship between $\Delta^{30}Si_{solid-water}$ values and temperature. The largest solid–water fractionation (−3.7‰, locally even up to −4.4‰) was found where stream-water temperatures were low (ca. 20 °C), and the smallest fractionation (−0.7‰) at the highest temperature (ca. 80 °C). Values for the spring pools (ca. 70°–100 °C) fit into this trend (−0.3 to −2.1‰) but show considerable variability, presumably due to deviating precipitation dynamics under different flow regimes.

Since precipitation occurs in a highly supersaturated regime, far from equilibrium concentrations (cf., DePaolo, 2011), the δ^{30}Si differences between sinter and fluid are attributable to effects of kinetic isotopic fractionation and/or steps in the fractionation pathway that are a function of temperature. These findings are qualitatively consistent with experimental results of Geilert et al. (2014) who determined $\Delta^{30}Si_{solid-water}$ values for precipitation from an oversaturated flowing solution in the same temperature range and also demonstrated temperature dependence for apparent kinetic fractionation. However, although in both

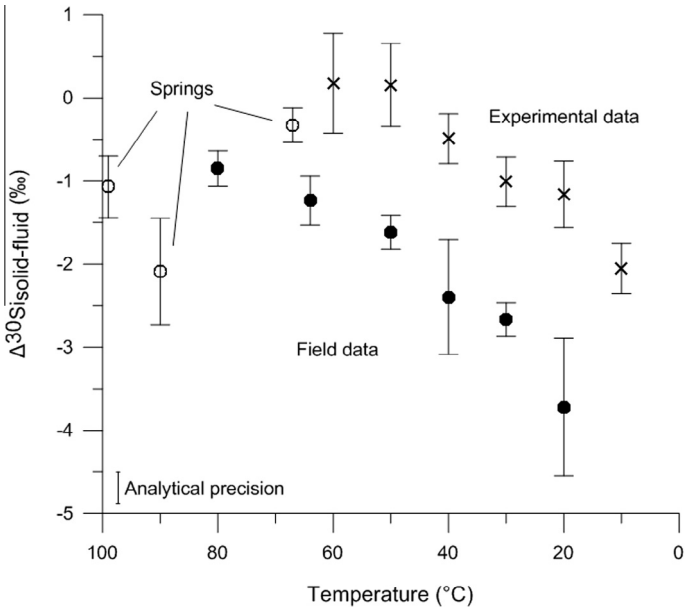

Fig. 9. Averaged $\Delta^{30}Si_{solid-water}$ values for sinter-water pairs from Geysir, Háihver, and Konungshver, plotted against temperature. Data from flow-through experiments representing steady-state conditions are shown for comparison (Geilert et al., 2014). Note that the trends demonstrate a similar dependency of the fractionation on temperature with an offset of ca. 2‰, if the spring waters (empty circles) are ignored. Error bars indicate uncertainties on average $\Delta^{30}Si_{solid-water}$ of replicates at approximately the same temperatures.

cases the precipitating solid is preferentially enriched in ^{28}Si, the values from the hot spring streams are considerably more negative than those from the experiments (Fig. 9). This larger fractionation in the natural streams and the near constancy in the $\Delta^{30}Si_{solid-water}$ offset argue for a control of silicon isotope fractionation other than temperature alone.

Insight into potential controlling factor(s) comes from a recent experimental study by Roerdink et al. (2015) who used the surface kinetic model of DePaolo (2011) to derive fractionation factors for precipitation of amorphous silica from supersaturated solutions at temperatures of 10–35 °C and pH 7.5–8.5. The authors found that the magnitude of solid–fluid fractionation decreased with decreasing precipitation rate in the course of individual batch experiments, which they attributed to a transition between kinetically dominated to equilibrium dominated fractionation behavior. Fractionation appeared to be temperature dependent with modeled kinetic fractionation factors ranging from −0.7 at 35 °C to −3.5‰ at 10 °C, whereas equilibrium fractionation factors were much smaller and varied only from –0.5 to +0.5‰ for these temperatures. Oelze et al. (2014) inferred a similar competition between kinetic and equilibrium fractionation in experiments on the absorption of silica onto crystalline gibbsite.

Within such a surface kinetic concept, the large magnitudes of apparent fractionation in the Geysir streams are in agreement with a kinetic dominated regime where fractionation is primarily controlled by the precipitation rate. As Fig. 10 illustrates, the magnitude of isotopic fractionation decreases (i.e. $\Delta^{30}Si_{solid-water}$ becomes less negative) with increasing precipitation rate, calculated according to the theoretically based scheme of Rimstidt and Barnes (1980), assuming an A/M value of 0.1 for each of the three streams. The dependence of the precipitation rate on temperature and saturation state explains why these parameters also correlate with the magnitude of isotopic fractionation.

5.5.1. Comparison with laboratory experiments

Our field-based data show similar systematics as the results from flow-through experiments of Geilert et al. (2014), but there is a significant offset in $\Delta^{30}Si_{solid-water}$ of 1.9‰ for the overlapping 20–60 °C temperature interval (Fig. 9) as well as in precipitation rates, which are lower than in the experiments (calculated for $A/M = 1000$; Fig. 10). We will first discuss the offset in the precipitation rates and then explore possible causes of the stronger isotopic fractionation in the stream waters.

The shift of approximately four orders of magnitude between the field and experimental results might be due to an underestimation of calculated precipitation rates for the streams. As mentioned above, theoretical models such as the one of Rimstidt and Barnes (1980) tend to yield several orders or magnitude slower precipitation rates than actual field rates. However, the same model was used to calculate the field and experimental rates shown in Fig. 10. We therefore assume that the uncertainty in A/M values adopted, which have a strong effect on the outcome of the rate calculations, is a more plausible reason. For example, the streambeds were assumed to be flat, whereas irregularities, biofilms and enhanced porosity accompanying loose packing of particles are more realistic and would strongly increase the reactive surface area and thus the A/M ratios. Hence, precipitation rates in the streams would be much higher if a more realistic surface area could be taken into account.

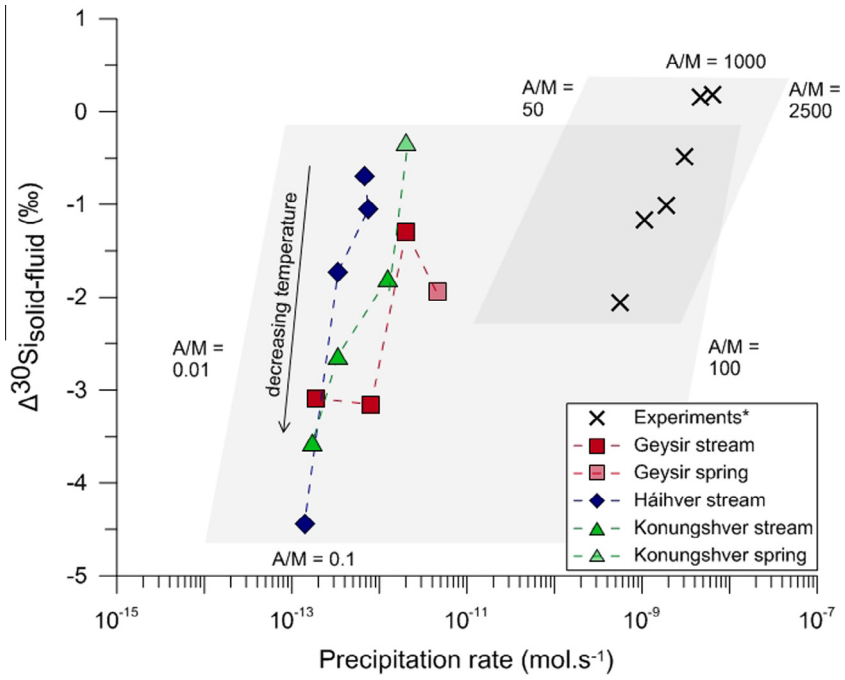

Fig. 10. Magnitudes of solid–water Si isotope fractionation ($\Delta^{30}Si_{solid-water}$) plotted against calculated precipitation rate (following Rimstidt and Barnes, 1980) for the Geysir, Háihver, and Konungshver systems. Experimentally determined steady-state $\Delta^{30}Si_{solid-water}$ values (Geilert et al., 2014) are shown for comparison. Note that both the natural systems and the experiments demonstrate an increase in the magnitude of silicon isotope fractionation (more negative $\Delta^{30}Si_{solid-water}$ values) with decreasing precipitation rates. Gray fields illustrate possible ranges in precipitation rates depending on allowable variations in adopted values for A/M ratios (0.01–100 and 50–2500 for the hot springs and experiments, respectively). Because the fields overlap, it is conceivable that the combined range of $\Delta^{30}Si_{solid-water}$ values is due to the effect of precipitation rate alone. See text for further discussion. Note that the data point for the Háihver spring is not shown due to its silica undersaturation, resulting in a negative precipitation rate.

Furthermore, the geothermal waters and the ultra-pure water-based solutions used in the experiments of Geilert et al. (2014) differed in pH, salinity and presence of impurities such as Al. Salinity and pH variations could exert a strong influence on the associated rate constants, by controlling the density of ionized surface silanol groups and the amorphous silica solubility (Rimstidt and Barnes, 1980; Weres et al., 1981; Carroll et al., 1998). Aluminum decreases silica solubility, and its incorporation in the precipitating phase can cause surface defects and might therefore significantly influence reaction kinetics (Iler, 1979; Weres et al., 1981; Carroll et al., 1998). Consequently, since salinity, pH and Al content will affect precipitation rates (Carroll et al., 1998), these factors along with the A/M uncertainties hamper an unambiguous comparison. Nonetheless, the first-order correspondence with the experimental results supports the evidence for a relationship between precipitation rate and Si isotope fractionation during steady-state deposition of sinter from the stream waters.

The higher pH and more complex chemistry of the stream waters compared to the experimental solutions could provide an explanation for the observed stronger isotopic fractionation. It is conceivable that the contrasting fractionation magnitudes are related to differences in the distribution of silica species present in solution. At the higher pH values of the hot spring waters (8.89–9.78), monomeric silica [H_4SiO_4(aq)] may be accompanied by its deprotonated equivalent [$H_3SiO_4^-$(aq)] since the pKa of monomeric silica is ca. 9.9 (Iler, 1979), whereas it will be the only relevant species at the near neutral pH in the experiments of Geilert et al. (2014). Recently, Dupuis et al. (2015) inferred a significant equilibrium fractionation of $-1.6 \pm 0.3‰$ between $H_3SiO_4^-$(aq) and H_4SiO_4(aq) at 300 K, based on a theoretical approach involving simulations of the aqueous species by *ab initio* molecular dynamics. Considering this large fractionation effect, the authors propose that speciation may have an important impact on solid–fluid Si isotope fractionation since the proton exchange required to transform one aqueous species into the other proceeds easily and thus promotes their isotopic equilibrium within the solution. However, the disparity between the field and experimentally derived solid–fluid fractionation values (Fig. 9) is difficult to attribute to fractionation among these monomeric aqueous species, as it would imply preferential removal of the isotopically lighter $H_3SiO_4^-$(aq) during precipitation. This seems unlikely in view of the concomitant increase in silica solubility and abundance of this species with increasing pH at pH > ca. 8.5 (e.g., Iler, 1979).

Finally, it is important to note that the magnitude of apparent isotopic fractionation decreases with increasing precipitation rate both in the Geysir streams and in the flow-through experiments of Geilert et al. (2014), whereas it decreases with decreasing precipitation rate in the

experiments of Oelze et al. (2014) and Roerdink et al. (2015). If this contrast is real and not a result of the dissimilar approaches for determining the rates, it can be explained by the difference in precipitation regimes. In the two latter sets of experiments, the relationship applies to instantaneous fractionation during precipitation in batch of fluid at a pre-set temperature, wherein isotope exchange is governed by a gradual transition from largely unidirectional kinetic effects during initially fast precipitation of silica to conditions when equilibrium is approached and reaction rates are reduced. In the field setting and in the experiments of Geilert et al. (2014) fractionation is associated with silica removal from a flowing solution at steady state under continuous supply of fluid with a constant Si content. In this case, the degree of supersaturation at a given sampling point remains constant with time, only depending on temperature and the concentration of dissolved silica in the source fluid.

When applying the conceptual surface kinetic model of DePaolo (2011) to the Geysir streams, the observed fractionation, expressed as $\Delta^{30}Si_{solid-water}$, is the net effect of kinetic and equilibrium processes each having their own fractionation characteristics that are associated with forward (precipitation) and backward (re-dissolution) Si fluxes at the solid–water interface. According to the findings of Roerdink et al. (2015), the magnitude of kinetic fractionation is high (up to ca. −3.5‰) whereas it is close to zero for equilibrium fractionation. According to these schematics, the lower fractionation magnitudes at the high temperatures close to the springs reflect fractionation behavior closer to equilibrium, while at the lower temperatures downstream where forward and backward rates are more out of balance, kinetic fractionation behavior prevails.

5.6. Geochemical implications

Douthitt (1982) already proposed that precipitation of opal from cooling and evaporating hot spring waters must be associated with a large isotopic fractionation. Considering the most extreme δ^{30}Si values for opaline sinter and hot spring water in the data from worldwide locations available at that time, the author postulated a maximum value for kinetic fractionation during low-temperature precipitation of −3.5‰. The apparent solid–water silicon isotope fractionations between ca. −0.1 and −4‰ found here for the Geysir area are derived from co-existing phases and extend toward much more negative values than observed so far for abiotic processes in most natural systems, which generally do not exceed −2‰ (Douthitt, 1982; Ding et al., 1996; Ziegler et al., 2005a; Georg et al., 2007a; Opfergelt et al., 2009, 2010, 2012). This fractionation variability has resulted in deposits of amorphous silica with a significant range of primary Si isotope signatures (δ^{30}Si between −0.1 and −4‰) that include some of the most negative values found in abiotic terrestrial materials to date. Only silicon isotope signatures of quartz of pedogenic and groundwater silcretes reach similar degrees of ^{30}Si depletion (mean δ^{30}Si values between −5.7‰ and −0.1‰; Basile-Doelsch et al., 2005). The authors argued that multiple dissolution-precipitation steps were required to create the most negative values, and proposed that reprecipitated quartz, produced during low-temperature silicification of surficial materials, represents an important terrestrial pool of depleted ^{30}Si that balances the enrichment in marine and river water relative to the reservoir of pristine igneous rocks.

The data from the Geysir sinter deposits presented here have several important implications that are relevant for the use of silicon isotopes for paleo-environmental reconstructions and in assessing sources and fluxes in the global silicon cycle:

(1) Chemical deposition from a supersaturated flowing solution can produce amorphous silica (opal-A) with highly diverse Si isotope compositions and variations over small distances, even if the parent fluid is virtually the same. Importantly, the observed isotopic diversity is a primary feature and is not induced by post-depositional diagenetic transformations of the silica, which, due to re-dissolution and precipitation steps involved, are likely to be associated with shifts in the original isotopic composition of opaline deposits (cf., Douthitt, 1982; Marin-Carbonne et al., 2014). Our findings illustrate the difficulty to extract pristine signatures of parent fluids from fossil equivalents of silica deposits as the ones studied here, even if superimposed diagenetic effects would be absent.
(2) Strongly negative δ^{30}Si signatures can be created in silica precipitates directly during deposition from a fluid, without the necessity of repeated re-dissolution-precipitation. Kinetic fractionation in an open system with continuous and unlimited supply of dissolved silicon seems a critical requirement since fractionation at equilibrium is probably very limited and Rayleigh-type fractionation during precipitation in a confined reservoir would raise the δ^{30}Si both in the dissolved silica and in the condensed phase when precipitation proceeds.
(3) The effective silicon isotope fractionation during precipitation from a saturated flowing solution in natural environments cannot be considered as constant but will be critically dependent on the properties of the system. Our field observations and comparison with experimental results (Geilert et al., 2014) suggest that precipitation rates exert a strong control on kinetic fractionation. Because the precipitation rate of amorphous silica is a function of temperature, saturation state, and the ratio of the solid–fluid interfacial area and water mass (A/M, Section 3.3), system properties will determine the magnitude of Si isotope fractionation to a major extent. For example, in the case of a hydrothermal system it is to be expected that effective fractionation will depend on local factors such as the geothermal gradient, the velocity of the ascending fluid and whether it flows in open conduits or through the pores of lithologies with limited permeability. Support for the critical control of system properties on fractionation behavior comes from recent experimental studies on Si precipitation (Roerdink et al., 2015) and Si adsorption onto

crystalline gibbsite (Oelze et al., 2014), which highlight the importance of reaction rates for cases where a batch of fluid evolves in a confined volume. This inferred relationship between kinetic Si isotope fractionation and precipitation rate opens up scope for using Si isotope data from siliceous deposits as a tracer of water-rock ratios (W/R), given that the precipitation rate depends on A/M which is convertible into W/R if the geometry of the system at issue can be reasonably constrained.

(4) Silica deposits from hydrothermal fluids may represent a significant non-biogenic terrestrial pool of light Si stored in solid material, next to the quartz cements of silcretes, clays and soils (Douthitt, 1982; Basile-Doelsch et al., 2005; Ziegler et al., 2005a,b; Georg et al., 2007a, 2009; Bern et al., 2010; Cornelis et al., 2010; Opfergelt et al., 2010; Steinhoefel et al., 2011). Pristine hydrothermal fluids probably acquire isotopic signatures close to those of the igneous rocks during interaction/dissolution at high temperatures, but subsequent precipitation of amorphous silica at lower temperatures will lead to the loss of relatively light silica from the solution. Our observations support this scenario, since, compared to compositions of typical Icelandic lavas, which average around −0.3‰ (Savage et al., 2011), the Geysir geothermal waters are enriched and the silica sinters depleted in ^{30}Si.

The δ^{30}Si values of dissolved silicon in Icelandic rivers are on average approximately +0.6‰, with a significant spread between −0.1 and +1.5‰ (Georg et al., 2007a; Opfergelt et al., 2013). Secondary clay formation and water runoff have been identified as main controls of riverine δ^{30}Si (Georg et al., 2007a), while diatom productivity in lakes (Opfergelt et al., 2011), a glaciated versus non-glaciated character of catchments (Opfergelt et al., 2013), and variable contributions from soil solutions (Pogge von Strandmann et al., 2012) have been proposed as other factors that potentially add to Si isotope variability of Icelandic river waters. The stream waters of the three Geysir aprons with their relatively uniform positive δ^{30}Si values (average 0.2‰) suggest that discharging geothermal waters represent an additional source of ^{30}Si-enriched fluids to the budgets of riverine silicon in Iceland.

Collectively, the available Si isotope data for terrestrial hydrothermal waters (δ^{30}Si of springs and streams between −0.2‰ and +1.6‰; Douthitt, 1982; Ding et al., 1996; Opfergelt et al., 2011, 2013; this work) overlap the lower end of the global range for rivers and lakes (δ^{30}Si between −0.1 and +3.4‰, Opfergelt and Delmelle, 2012 and references therein). Although the proportion of hydrothermal water in the global terrestrial run-off is modest, the enhanced concentrations of cations in rivers draining volcanic regions (e.g., Dessert et al., 2009) lend support to the hypothesis that active geothermal systems hosted by igneous lithologies may be a more important contributor to the Si isotope signature of continent-derived fluxes of silicon to the oceans than has been realized so far. Further work is needed to verify this.

5.7. Implications for the Si isotope signals of Precambrian cherts

The above mentioned corollaries 1–3 may have consequences for the interpretation of silicon isotope signatures of ancient silica-rich deposits in terms of paleo-environmental conditions. They are relevant in valuing the significance of Si isotopes of Precambrian cherts as a potential record of paleo-ocean temperatures (see Marin-Carbonne et al., 2014 for a recent review), particularly if the cherts formed by direct abiotic chemical precipitation from saturated seawater or hydrothermal fluids venting at the seafloor (referred to as C-cherts by Van den Boorn et al., 2007), i.e. in a similar way as the Geysir sinters. Interpretations are not straightforward because the isotopic variabilities measured in these cherts can have multiple causes. Among the proposed explanations are changes in seawater temperatures, variations in the provenance of dissolved silica, differences in the mechanism of silica precipitation, Rayleigh-type fractionations within pore waters, and post-depositional, fluid-driven modifications during diagenesis or metamorphism (Robert and Chaussidon, 2006; Van den Boorn et al., 2007, 2010; Marin et al., 2010; Chakrabarti et al., 2012; Marin-Carbonne et al., 2014). Isotopic variability in chert samples on micrometer scale has been attributed to the stepwise transformation of the amorphous silica precursor into microcrystalline quartz during diagenesis, whereby local heterogeneities have been preserved (Marin et al., 2010; Marin-Carbonne et al., 2014).

A key uncertainty in reconstructing paleo-environmental and diagenetic conditions has been the lack of quantitative data on Si isotope fractionation. Since amorphous silica (opal-A), precipitated from a saturated solution, was probably the precursor of the microcrystalline quartz of Precambrian C-cherts (e.g., Knauth, 1994), our findings demonstrate that Si isotope fractionation cannot be taken as a universally applicable constant in data interpretations but should be regarded as a system-dependent variable associated with the precipitation rate. In fact, at temperatures less than 100 °C, the effective kinetic fractionation during precipitation of the precursor silica from a free-flowing fluid induced by a temperature drop (e.g., hydrothermal fluids venting at the seafloor, circulating seawater, fluids in subsurface veins and other open conduits) may range anywhere between ca. 0 and −4‰ (see Fig. 9). If formation conditions as these apply, derivation of paleo-temperatures from the isotopic signatures of orthochemical chert, which relies on an assumption for the fractionation factor, is complicated by the temperature dependence of the precipitation rate. Our observations thus question the validity of taking effective Si isotope fractionation to be temperature independent, as is usually rationalized with reference to the very minor change in the fractionation between quartz and fluid of about 0.1‰/10 °C, predicted from first-principles density-functional theory for equilibrium fractionation (Méheut et al., 2007, 2009).

In practical interpretations of field data, it can be difficult to distinguish the role of temperature from other

factors that contribute to the precipitation rate and thus to the magnitude of kinetic Si isotope fractionation. The following example illustrates this for a set of cherts that formed by silicification of a precursor rock (S-cherts of Van den Boorn et al., 2007). In a study of Archean submarine basalts in the Barberton Greenstone Belt, Abraham et al. (2011) documented trends in Si isotope signatures in meter-scale sections between pristine internal parts of basalt and highly silicified outer parts near the inferred former interface with seawater. The authors explained the observed δ^{30}Si trends with a seawater percolation model invoking temperature-dependent fluid-solid Si-isotope fractionation which would have been strong at relatively low temperatures near the seawater interface and modest in the internal parts of the sections where temperatures had been higher. Instead, we surmise that the assumed change in the degree of fractionation reflects a transition in *W/R* ratios, at least partially, as abundant cracks and veins in the outer parts of the basalts point to higher *W/R* ratios (equivalent to lower *A/M*), hence stronger fractionation, than in the internal parts where veining is less or absent and fluid circulation was presumably more controlled by porosity and grain-boundary processes.

As a final note, it should be emphasized that fractionation magnitudes in open systems with free flowing fluid are likely to deviate from those under closed-system conditions, as might be imposed during the diagenetic transformations from opal-A to quartz if the accompanying dissolution-precipitation reactions take place in reducing pore spaces of the siliceous sediment (Marin-Carbonne et al., 2014). Therefore, secondary isotope shifts acquired during post-depositional diagenesis will be governed by different, relatively modest fractionation magnitudes.

6. SUMMARY AND CONCLUSIONS

Silicon isotope compositions were determined in waters and associated silica sinters from three hot spring systems of the Geysir geothermal field with the objective to explore isotopic fractionation in a natural setting with active precipitation from a saturated solution.

The SiO_2 concentrations in the spring and stream waters ranged from 290 to 560 ppm and stayed relatively constant along downstream trajectories, irrespective of significant cooling gradients. Except for the Háihver pool, the waters were always supersaturated with respect to amorphous silica at the temperatures measured in the field. Correlations between the saturation indices, temperature and amounts of evaporative water loss suggest that cooling and evaporation were the main causes of subaqueous silica precipitation.

The δ^{30}Si values for the waters averaged around +0.2‰ and stayed relatively constant, due to the small quantities of instantaneously precipitating silica relative to the dissolved amount. The δ^{30}Si values for silica sinters deposited in the streambeds were systematically lower than the corresponding water values, consistent with preferential incorporation of the lighter silicon isotope in the solid during fractionation. The sinter values ranged from −0.1‰ to −4.0‰, and showed a downstream decrease with increasing distance to the vent in all three systems.

Assuming that the isotopic compositions of co-existing waters and sinters are products of current conditions at each of the sampling sites along the streams, there is a strong correlation between solid–water fractionation and temperature, with average $\Delta^{30}Si_{solid-water}$ increasing from ca. −0.7‰ at ~80 °C to −3.7‰ at ~20 °C. The inferred temperature relationship is almost identical to that observed in flow-through experiments (Geilert et al., 2014), but shows a systematic offset between the $\Delta^{30}Si_{solid-water}$ values of ca. −2‰ at a given temperature, with the natural samples showing the larger fractionation magnitude. This observation and the constancy in the $\Delta^{30}Si_{solid-water}$ offset suggest that silicon isotope fractionation during precipitation from a continuously supplied flowing fluid is not only controlled by temperature. Instead, we propose that the precipitation rates of amorphous silica play a critical role, with the magnitude of solid–water silicon isotopic fractionation decreasing with increasing rate. We conclude that system properties and their potential effects on isotopic fractionation must be taken into account when interpreting silicon isotope signatures in recent and ancient silica rich deposits.

ACKNOWLEDGMENTS

We thank Helen de Waard, Bas van der Wagt and Richard Smeets for technical support in the Utrecht and Amsterdam Laboratories, and Jóhann Gunnarsson Robin for his help in the field. Our manuscript benefitted from critical and constructive comments of three anonymous reviewers. This project was partly financially supported by the Netherlands Organisation for Scientific Research (NWO-ALW), project no. 819.01.005. The MC-ICPMS facility was supported by a grant (175.107.404.01) from NWO-ALW.

REFERENCES

Abraham K., Hofmann A., Foley S. F., Cardinal D., Harris C., Barth M. G. and André L. (2011) Coupled silicon-oxygen isotope fractionation traces Archaean silicification. *Earth Planet. Sci. Lett.* **301**, 222–230.

André L., Cardinal D., Alleman L. Y. and Moorbath S. (2006) Silicon isotopes in ~3.8 Ga West Greenland rocks as clues to the Eoarchaean supracrustal Si cycle. *Earth Planet. Sci. Lett.* **245**, 162–173.

Arnórsson S. (1985) The use of mixing models and chemical geothermometers for estimating underground temperatures in geothermal systems. *J. Volcanol. Geoth. Res.* **23**, 299–335.

Arnórsson S. and Andrésdóttir A. (1995) Processes controlling the distribution of boron and chlorine in natural waters in Iceland. *Geochim. Cosmochim. Acta* **59**, 4125–4146.

Arnórsson S., Bjarnason J. Ö., Giroud N., Gunnarsson I. and Stefánsson A. (2006) Sampling and analysis of geothermal waters. *Geowaters* **6**, 203–216.

Basile-Doelsch I. (2006) Si stable isotopes in the Earth's surface. a review. *J. Geochem. Explor.* **88**, 252–256.

Basile-Doelsch I., Meunier J. D. and Parron C. (2005) Another continental pool in the terrestrial silicon cycle. *Nature* **433**, 399–402.

Bern C., Brzezinski M., Beucher C., Ziegler K. and Chadwick O. (2010) Weathering, dust, and biocycling effects on soil silicon isotope ratios. *Geochim. Cosmochim. Acta* **74**, 876–889.

Braunstein D. and Lowe D. R. (2001) Relationship between spring and geyser activity and the deposition and morphology of high temperature (>73 °C) siliceous sinter, Yellowstone National Park, Wyoming, USA. *J. Sediment. Res.* **71**, 747–763.

Campbell K. A., Sannazzaro K., Rodgers K. A., Herdianita N. R. and Browne P. R. L. (2001) Sedimentary facies and mineralogy of the Late Pleistocene Umukuri silica sinter, Taupo Volcanic Zone, New Zealand. *J. Sediment. Res.* **71**, 727–746.

Cardinal D., Gaillardet J., Hughes H. J., Opfergelt S. and André L. (2010) Contrasting silicon isotope signatures in rivers from the Congo Basin and the specific behaviour of organic-rich waters. *Geophys. Res. Lett.* **37**, L12403.

Carroll S., Mroczek E., Alai M. and Ebert M. (1998) Amorphous silica precipitation (60 to 120 °C): comparison of laboratory and field rates. *Geochim. Cosmochim. Acta* **62**, 1379–1396.

Chafetz H. S. and Lawrence J. R. (1994) Stable isotopic variability within modern travertines. *Géog. Phys. Quatern.* **48**, 257–273.

Chakrabarti R., Knoll A. H., Jacobsen S. B. and Fischer W. W. (2012) Si isotope variability in Proterozoic cherts. *Geochim. Cosmochim. Acta* **91**, 187–201.

Channing A. and Butler I. B. (2007) Cryogenic opal-A deposition from Yellowstone hot springs. *Earth Planet. Sci. Lett.* **257**, 121–131.

Clayton R. N., O'Neil J. R. and Mayeda T. K. (1972) Oxygen isotope exchange between quartz and water. *J. Geophys. Res.*, 77.

Conley D. J. (2002) Terrestrial ecosystems and the global biogeochemical silica cycle. *Global Biogeochem. Cycles* **16**, 1121.

Cornelis J.-T., Delvaux B., Cardinal D., André L., Ranger R. and Opfergelt S. (2010) Tracing mechanisms controlling the release of dissolved silicon in forest soil solutions using Si isotopes and Ge/Si ratios. *Geochim. Cosmochim. Acta* **74**, 3913–3924.

Cornelis J. T., Delvaux B., Georg R. B., Lucas Y., Ranger R. and Opfergelt S. (2011) Tracing the origin of dissolved silicon transferred from various soil-plant systems towards rivers: a review. *Biogeosciences* **8**, 89–112.

Cornelis J. T., Weis D., Lavkulich L., Vermeire M.-L., Delvaux D. and Barling J. (2014) Silicon isotopes record dissolution and re-precipitation of pedogenic clay minerals in a podzolic soil chronosequence. *Geoderma* **235–236**, 19–29.

Craig H. (1961) Isotopic variations in meteoric waters. *Science* **133**, 1702–1703.

De La Rocha C. L., Brezinski M. A. and DeNiro M. J. (2000) A first look at the distribution of the stable isotopes of silicon in natural waters. *Geochim. Cosmochim. Acta* **64**, 2467–2477.

Delstanche S., Opfergelt S., Cardinal D., Elsass F., André L. and Delvaux B. (2009) Silicon isotopic fractionation during adsorption of aqueous monosilicic acid onto iron oxide. *Geochim. Cosmochim. Acta* **73**, 923–934.

Delvigne C., Cardinal D., Hofmann A. and André L. (2012) Stratigraphic changes of Ge/Si, REE+Y and silicon isotopes as insights into the deposition of a Mesoarchaean banded iron formation. *Earth Planet. Sci. Lett.* **355–356**, 109–118.

DePaolo D. J. (2011) Surface kinetic model for isotopic and trace element fractionation during precipitation of calcite from aqueous solutions. *Geochim. Cosmochim. Acta* **75**, 1039–1056.

Dessert C., Gaillardet J., Dupre B., Schott J. and Pokrovsky O. S. (2009) Fluxes of high- versus low-temperature water–rock interactionsin aerial volcanic areas: example from the Kamchatka Peninsula, Russia. *Geochim. Cosmochim. Acta* **73**, 148–169.

Ding T. P., Jiang S., Wan D., Li Y., Li J., Song H., Liu Z. and Yao X. (1996) *Silicon isotope geochemistry*. Geological Publishing, Beijing.

Ding T. P., Wan D., Wang C. Y. and Zhang F. (2004) Silicon isotope compositions of dissolved silicon and suspended matter in the Yangtze River, China. *Geochim. Cosmochim. Acta* **68**, 205–216.

Ding T. P., Gao J. F., Tian S. H., Wang H. B. and Li M. (2011) Silicon isotopic composition of dissolved silicon and suspended particulate matter in the Yellow River, China, with implications for the global silicon cycle. *Geochim. Cosmochim. Acta* **75**, 6672–6689.

Douthitt C. B. (1982) The geochemistry of the stable isotopes of silicon. *Geochim. Cosmochim. Acta* **46**, 1449–1458.

Dupuis R., Benoit M., Nardin E. and Méheut M. (2015) Fractionation of silicon isotopes in liquids: the importance of configurational disorder. *Chem. Geol.* **396**, 239–254.

Engström E., Rodushkin I., Ingri J., Baxter D. C., Ecke F., Österlund H. and Öhlander B. (2010) Temporal isotopic variations of dissolved silicon in a pristine boreal river. *Chem. Geol.* **271**, 142–152.

Fournier R. O. (1985) The behaviour of silica in hydrothermal solutions. Geology and geochemistry of epithermal systems. *Rev. Econ. Geol.* **2**, 45–60.

Fournier R. O. and Rowe J. J. (1966) Estimation of underground temperatures from the silica content of water from hot springs and wet-steam wells. *Am. J. Sci.* **264**, 685–697.

Geilert S., Vroon P. Z., Roerdink D. L., Van Cappellen P. and van Bergen M. J. (2014) Silicon isotope fractionation during abiotic silica precipitation at low temperatures: inferences from flow-through experiments. *Geochim. Cosmochim. Acta* **142**, 95–114.

Georg R. B., Reynolds B. C., Frank M. and Halliday A. N. (2006) Mechanisms controlling the silicon isotopic compositions of river waters. *Earth Planet. Sci. Lett.* **249**, 290–306.

Georg R. B., Reynolds B. C., West A. J., Burton K. W. and Halliday A. N. (2007a) Silicon isotope variations accompanying basalt weathering in Iceland. *Earth Planet. Sci. Lett.* **261**, 476–490.

Georg R. B., Halliday A. N., Schauble E. A. and Reynolds B. C. (2007b) Silicon in the Earth's core. *Nature* **447**, 1102–1106.

Georg R. B., Zhu C., Reynolds B. C. and Halliday A. N. (2009) Stable silicon isotopes of groundwater, feldspars, and clay coatings in the Navajo Sandstone aquifer, Black Mesa, Arizona, USA. *Geochim. Cosmochim. Acta* **73**, 2229–2241.

Guidry S. A. and Chafetz H. S. (2002) Factors governing subaqueous siliceous sinter precipitation in hot springs: examples from Yellowstone National Park, USA. *Sedimentology* **49**, 1253–1267.

Guidry S. A. and Chafetz H. S. (2003a) Anatomy of siliceous hot springs: examples from Yellowstone National Park, Wyoming, USA. *Sed. Geol.* **157**, 71–106.

Guidry S. A. and Chafetz H. S. (2003b) Depositional facies and diagenetic alteration in a relict siliceous hot-spring accumulation: examples from Yellowstone National Park, U.S.A. *J. Sediment. Res.* **73**, 806–823.

Gunnarsson I. and Arnórsson S. (2000) Amorphous silica solubility and the thermodynamic properties of H_4SiO_4 in the range of 0 to 350 °C at P_{sat}. *Geochim. Cosmochim. Acta* **64**, 2295–2307.

Handley K. M., Campbell K. A., Mountain B. W. and Browne P. R. L. (2005) Abiotic-biotic controls on the origin and development of spicular sinter: in situ growth experiments, Champagne Pool, Waiotapu, New Zealand. *Geobiology* **3**, 93–114.

Heck P. R., Huberty J. M., Kita N. T., Ushikubo T., Kozdon R. and Valley J. W. (2011) SIMS analyses of silicon and oxygen isotope ratios for quartz from Archean and Paleoproterozoic banded iron formations. *Geochim. Cosmochim. Acta* **75**, 5879–5891.

Herdianita N. R., Browne P. R. L., Rodgers K. A. and Campbell K. A. (2000) Mineralogical and textural changes accompanying ageing of silica sinter. *Miner. Deposita* **35**, 48–62.

Hinman N. W. and Lindstrom R. F. (1996) Seasonal changes in silica deposition in hot springs systems. *Chem. Geol.* **132**, 237–246.

Hughes H. J., Sondag F., Santos R. V., André L. and Cardinal D. (2013) The riverine silicon isotope composition of the Amazon Basin. *Geochim. Cosmochim. Acta* **121**, 637–651.

Icopini G. A., Brantley S. L. and Heaney P. J. (2005) Kinetics of silica oligomerization and nanocolloid formation as a function of pH and ionic strength at 25 °C. *Geochim. Cosmochim. Acta* **69**, 293–303.

Iler R. K. (1979) *The Chemistry of Silica: Solubility, Polymerization, Colloid and Surface Chemistry, and Biochemistry*. John Wiley & Sons.

Jones B. and Renaut R. W. (2003) Hot spring and geyser sinters: the integrated product of precipitation, replacement, and deposition. *Can. J. Earth Sci.* **40**, 1549–1569.

Jones B. and Renaut R. W. (2010) Impact of seasonal changes on the formation and accumulation of soft siliceous sediments on the discharge apron of Geysir, Iceland. *J. Sediment. Res.* **80**, 17–35.

Jones B. and Segnit E. R. (1971) The nature of opal I: nomenclature and constituent phases. *J. Geol. Soc. Aust.* **18**, 57–68.

Kaasalainen H. and Stefánsson A. (2012) The chemistry of trace elements in surface geothermal waters and steam, Iceland. *Chem. Geol.* **330–331**, 60–85.

Kastner M., Keene J. B. and Gieskes J. M. (1977) Diagenesis of siliceous oozes-I. Chemical controls on the rate of opal-A to opal-CT transformation – an experimental study. *Geochim. Cosmochim. Acta* **41**, 1041–1059.

Kele S., Demény A., Siklósy Z., Németh T., Tóth M. and Kovács M. B. (2008) Chemical and stable isotope composition of recent hot-water travertines and associated thermal waters, from Egerszalók, Hungary: depositional facies and non-equilibrium fractionation. *Sed. Geol.* **211**, 53–72.

Kele S., Özkul M., Fórizs I., Gökgöz A., Baykara M. O., Alçiçek M. C. and Németh T. (2011) Stable isotope geochemical study of Pamukkale travertines: new evidences of low-temperature non-equilibrium calcite-water fractionation. *Sed. Geol.* **238**, 191–212.

Kempl J., Vroon P. Z., Zinngrebe E. and van Westrenen W. (2013) Si isotope fractionation between Si-poor metal and silicate melt at pressure–temperature conditions relevant to metal segregation in small planetary bodies. *Earth Planet. Sci. Lett.* **368**, 61–68.

Knauth L. P. (1994) Petrogenesis of chert. In *Silica: Physical Behavior, Geochemistry and Materials Applications* (eds. P. J. P. Heaney, C. T. Prewitt and G. V. Gibbs). Mineralogical Society of America, pp. 233–258.

Knauth L. P. and Epstein S. (1975) Hydrogen and oxygen isotope ratios in silica from the JOIDES Deep Sea Drilling Project. *Earth Planet. Sci. Lett.* **25**, 1–10.

Knauth L. P. and Epstein S. (1976) Hydrogen and oxygen isotope ratios innodular and bedded cherts. *Geochim. Cosmochim. Acta* **40**, 1095–1108.

Konhauser K. O. and Ferris F. G. (1996) Diversity of iron and silica precipitation by microbial mats in hydrothermal waters, Iceland: implications for Precambrian iron formations. *Geology* **24**, 323–326.

Konhauser K. O., Phoenix V. R., Bottrell S. H., Adams D. G. and Head I. M. (2001) Microbial-silica interactions in Icelandic hot spring sinter: possible analogues for some Precambrian siliceous stromatolites. *Sedimentology* **48**, 415–433.

Konhauser K. O., Jones B., Phoenix V. R., Ferris F. G. and Renaut R. W. (2004) The microbial role in hot spring silicification. *Ambio* **33**, 546–552.

Li Y., Ding T. and Wan D. (1995) Experimental study of silicon isotope dynamic fractionation and its application in geology. *Chin. J. Geochem.* **14**, 212–219.

Lynne B. Y. (2012) Mapping vent to distal-apron hot spring paleoflow pathways using siliceous sinter architecture. *Geothermics* **43**, 3–24.

Lynne B. Y. and Campbell K. A. (2003) Diagenetic transformations (opal-A to quartz) of low- and mid-temperature microbial textures in siliceous hot-spring deposits, Taupo Volcanic Zone, New Zealand. *Can. J. Earth Sci.* **40**, 1679–1696.

Lynne B. Y. and Campbell K. A. (2004) Morphologic and mineralogic transitions from opal-A to opal-CT in low-temperature siliceous sinter diagenesis, Taupovolcanic zone, New Zealand. *J. Sediment. Res.* **74**, 561–579.

Lynne B. Y., Campbell K. A., Moore J. N. and Browne P. R. L. (2005) Diagenesis of 1900-year-old siliceous sinter (opal-A to quartz) at Opal Mound, Roosevelt Hot Springs, Utah, U.S.A. *Sediment. Geol.* **179**, 249–278.

Lynne B. Y., Campbell K. A., Moore J. and Browne P. R. L. (2008) Origin and evolution of the Steamboat Springs siliceous sinter deposit, Nevada, U.S.A. *Sed. Geol.* **210**, 111–131.

Marin J., Chaussidon M. and Robert F. (2010) Microscale oxygen isotope variations in 1.9 Ga Gunflint cherts: assessments of diagenesis effects and implications for oceanic paleotemperature reconstructions. *Geochim. Cosmochim. Acta* **74**, 116–130.

Marin-Carbonne J., Chaussidon M., Boiron M. C. and Robert F. (2011) A combined in situ oxygen, silicon isotopic and water inclusion study of a chert sample from Onverwacht Group (3.35 Ga, South Africa): new constraints on water circulation. *Chem. Geol.* **286**, 59–71.

Marin-Carbonne J., Chaussidon M. and Robert F. (2012) Micrometer-scale chemical and isotopic criteria (O and Si) on the origin and history of Precambrian cherts: implications for paleo-temperature reconstructions. *Geochim. Cosmochim. Acta* **92**, 129–147.

Marin-Carbonne J., Robert F. and Chaussidon M. (2014) The silicon and oxygen isotope compositions of Precambrian cherts: a record of oceanic paleo-temperatures? *Precambr. Res.* **247**, 223–234.

Méheut M., Lazzeri M., Balan E. and Mauri F. (2007) Equilibrium isotopic fractionation in the kaolinite, quartz, water system: prediction from first-principles density-functional theory. *Geochim. Cosmochim. Acta* **71**, 3170–3181.

Méheut M., Lazzeri M., Balan E. and Mauri F. (2009) Structural control over equilibrium silicon and oxygen isotopic fractionation: a first-principles density-functional theory study. *Chem. Geol.* **258**, 28–37.

Mountain B. W., Benning L. G. and Boerema J. (2003) Experimental studies on New Zealand hot spring sinters: rates of growth and textural development. *Can. J. Earth Sci.* **40**, 1643–1667.

Nelson S. T. (2000) A simple, practical methodology for routine VSMOW/SLAP normalization of water samples analyzed by continuous flow methods. *Rapid Commun. Mass Spectrom.* **14**, 1044–1046.

Oelze M., von Blanckenburg F., Hoellen D., Dietzel M. and Bouchez J. (2014) Si stable isotope fractionation during adsorption and the competition between kinetic and equilibrium isotope fractionation: implications for weathering systems. *Chem. Geol.* **380**, 161–171.

Oelze M., von Blanckenburg F., Bouchez J., Hoellen D. and Dietzel M. (2015) The effect of Al on Si isotope fractionation investigated by silica precipitation experiments. *Chem. Geol.* **397**, 94–105.

Opfergelt S. and Delmelle P. (2012) Silicon isotopes and continental weathering processes: assessing controls on Si transfer to the ocean. *C.R. Geosci.* **344**, 723–738.

Opfergelt S., de Bournonville G., Cardinal D., André L., Delstanche S. and Delvaux B. (2009) Impact of soil weathering degree on silicon isotopic fractionation during adsorption onto iron oxides in basaltic ash soils, Cameroon. *Geochim. Cosmochim. Acta* **73**, 7226–7240.

Opfergelt S., Cardinal D., André L., Delvigne C., Bremond L. and Delvaux B. (2010) Variations of d^{30}Si and Ge/Si with weathering and biogenic input in tropical basaltic ash soils under monoculture. *Geochim. Cosmochim. Acta* **74**, 225–240.

Opfergelt S., Eiriksdottir E. S., Burton K. W., Einarsson A., Siebert C., Gislason S. R. and Halliday A. N. (2011) Quantifying the impact of freshwater diatom productivity on silicon isotopes and silicon fluxes: Lake Myvatn, Iceland. *Earth Planet. Sci. Lett.* **305**, 73–82.

Opfergelt S., Georg R. B., Delvaux B., Cabidoche Y., Burton K. W. and Halliday A. N. (2012) Silicon isotopes and the tracing of desilication in volcanic soil weathering sequences, Guadeloupe. *Chem. Geol.* **326–327**, 113–122.

Opfergelt S., Burton K. W., Pogge von Strandmann P. A. E., Gislason S. R. and Halliday A. N. (2013) Riverine silicon isotope variations in glaciated basaltic terrains: implications for the Si delivery to the ocean over glacial–interglacial intervals. *Earth Planet. Sci. Lett.* **369–370**, 211–219.

Orange F., Lalonde S. V. and Konhauser K. O. (2013) Experimental simulation of evaporation-driven silica sinter formation and microbial silicification in hot spring systems. *Astrobiology* **13**, 163–176.

Parkhurst D. L. and Appelo C. A. J. (1999) User's guide to PHREEQC (Version 2) – A computer program for speciation, batch-reaction, one-dimensional transport, and inverse geochemical calculations: U.S. Geological Survey Water-Resources Investigations Report. pp. 99–4259.

Pogge von Strandmann P. A. E., Opfergelt S., Lai Y., Sigfússon B., Gislason S. R. and Burton K. W. (2012) Lithium, magnesium and silicon isotope behaviour accompanying weathering in a basaltic soil and pore water profile in Iceland. *Earth Planet. Sci. Lett.* **339–340**, 11–23.

Potts Ph. J. (2012) A proposal for the publication of geochemical data in the scientific literature. *Geostand. Geoanal. Res.* **36**, 225–230.

Renaut R. W. and Jones B. (2003) Sedimentology of hot spring systems. *Can. J. Earth Sci.* **40**, 1439–1442.

Renders P. J. N., Gammons C. H. and Barnes H. L. (1995) Precipitation and dissolution rate constants for cristobalite from 150 to 300 °C. *Geochim. Cosmochim. Acta* **59**, 77–85.

Rice C. M., Ashcroft W. A., Batten D. J., Boyce A. J., Caulfied J. B. D., Fallick A. E., Hole M. J., Jones E., Pearson M. J., Rogers G., Saxton J. M., Stuart F. M., Trewin N. H. and Turner G. (1995) A Devonian auriferous hot spring system, Rhynie, Scotland: London. *J. Geol. Soc.* **152**, 229–250.

Rimstidt J. D. and Barnes H. L. (1980) The kinetics of silica-water reactions. *Geochim. Cosmochim. Acta* **44**, 1683–1699.

Robert F. and Chaussidon M. (2006) A paleotemperature curve for the Precambrian oceans based on silicon isotopes in cherts. *Nature* **443**, 969–972.

Rodgers K. A., Browne P. R. L., Buddle T. F., Cook K. L., Greatrex R. A., Hampton W. A., Herdianita N. R., Holland G. R., Lynne B. Y., Martin R., Newton Z., Pastars D., Sannazarro K. L. and Teece C. I. A. (2004) Silica phases in sinters and residues from geothermal fields of New Zealand. *Earth Sci. Rev.* **66**, 1–61.

Roerdink D. L., van den Boorn S. H. J. M., Geilert S., Vroon P. Z. and van Bergen M. J. (2015) Experimental constraints on kinetic and equilibrium silicon isotope fractionation during the formation of non-biogenic chert deposits. *Chem. Geol.* **402**, 40–51.

Rothbaum H. P. and Rohde A. G. (1979) Kinetics of silica polymerization and deposition from dilute solutions between 5 and 180 °C. *J. Colloid Interface Sci.* **71**, 533–559.

Savage P. S., Georg R. B., Armytage R. M. G., Williams H. M. and Halliday A. N. (2010) Silicon isotope homogeneity in the mantle. *Earth Planet. Sci. Lett.* **295**, 139–146.

Savage P. S., Georg R. B., Williams H. M., Burton K. W. and Halliday A. N. (2011) Silicon isotope fractionation during magmatic differentiation. *Geochim. Cosmochim. Acta* **75**, 6124–6139.

Savage P. S., Georg R. B., Williams H. M. and Halliday A. N. (2013) The silicon isotope composition of the upper continental crust. *Geochim. Cosmochim. Acta* **109**, 384–399.

Steinhoefel G., Horn I. and von Blanckenburg F. (2009) Micro-scale tracing of Fe and Si isotope signatures in banded iron formation using femtosecond laser ablation. *Geochim. Cosmochim. Acta* **73**, 5343–5360.

Steinhoefel G., von Blanckenburg F., Horn I., Konhauser K. O., Beukes N. J. and Gutzmer J. (2010) Deciphering formation processes of banded iron formations from the Transvaal and the Hamersley successions by combined Si and Fe isotope analysis using UV femtosecond laser ablation. *Geochim. Cosmochim. Acta* **74**, 2677–2696.

Steinhoefel G., Breuer J., Horn I., Kaczorek D. and Sommer M. (2011) Micrometer silicon isotope diagnostics of soils by UV femtosecond laser ablation. *Chem. Geol.* **286**, 280–289.

Tobler D. J. and Benning L. G. (2013) In situ and time resolved nucleation and growth of silica nanoparticles forming under simulated geothermal conditions. *Geochim. Cosmochim. Acta* **114**, 156–168.

Tobler D. J., Stefansson A. and Benning L. G. (2008) In situ grown silica sinters in Icelandic geothermal areas. *Geobiology* **6**, 481–502.

Tréguer P. and De La Rocha C. L. (2013) The world ocean silica cycle. *Annu. Rev. Mar. Sci.* **5**, 477–501.

Tréguer P., Nelson D. M., Van Bennekom A. J., DeMaster D. J., Leynaert A. and Quéguiner B. (1995) The silica balance in the world ocean: a reestimate. *Science* **268**, 375–379.

Van Cappellen P. and Qiu L. (1997) Biogenic silica dissolution in sediments of the Southern Ocean. I. Solubility. *Deep-Sea Res. II* **44**, 1109–1128.

Van den Boorn S. H. J. M., Vroon P. Z., Van Belle C. C., Van der Wagt B., Schwieters J. and Van Bergen M. J. (2006) Determination of silicon isotope ratios in silicate materials by high-resolution MC-ICP-MS using a sodium hydroxide sample digestion method. *J. Anal. At. Spectrom.* **21**, 734–742.

Van den Boorn S. H. J. M., Van Bergen M. J., Nijman W. and Vroon P. Z. (2007) Dual role of seawater and hydrothermal waters in Early Archaean chert formation: evidence from silicon isotopes. *Geology* **35**, 939–942.

Van den Boorn S. H. J. M., Vroon P. Z. and van Bergen M. J. (2009) Sulfur-induced offset in MC-ICP-MS silicon-isotopes measurements. *J. Anal. At. Spectrom.* **24**, 1111–1114.

Van den Boorn S. H. J. M., van Bergen M. J., Vroon P. Z., de Vries S. T. and Nijman W. (2010) Silicon isotope and trace element constraints on the origin of ~3.5 Ga cherts: implications for Early Archaean marine environments. *Geochim. Cosmochim. Acta* **74**, 1077–1103.

Weres O., Yee A. and Tsao L. (1981) Kinetics of silica polymerization. *J. Colloid Interface Sci.* **84**, 379–402.

White D. E., Brannock W. W. and Murata K. J. (1956) Silica in hot-spring waters. *Geochim. Cosmochim. Acta* **10**, 27–59.

Williams L. A. and Crerar D. A. (1985) Silica diagenesis, II. General mechanisms. *J. Sediment. Petrol.* **55**, 0312–0321.

Wollast R. and Mackenzie F. T. (1983) The global cycle of silica. In *Silicon Geochemistry and Biogeochemistry* (ed. S. R. Aston). Academic Press, London, pp. 39–76.

Zambardi T. and Poitrasson F. (2011) Precise determination of silicon isotopes in silicate rock reference materials by MC-ICP-MS. *Geostand. Geoanal. Res.* **35**, 89–99.

Ziegler K., Chadwick O. A., Brzezinski M. A. and Kelly E. F. (2005a) Natural variations of δ^{30}Si ratios during progressive basalt weathering, Hawaiian Islands. *Geochim. Cosmochim. Acta* **69**, 4597–4610.

Ziegler K., Chadwick O. A., White A. F. and Brzezinski M. A. (2005b) δ^{30}Si systematics in a granitic saprolite, Puerto Rico. *Geology* **33**, 817–820.

Associate editor: Jeffrey C. Alt